The Astrophysical Journal, 808:38 (30pp), 2015 July 20 doi:10.1088/0004-637X/808/1/38

DISSECTING THE GASEOUS HALOS OF $z \sim 2$ DAMPED Lyα SYSTEMS WITH CLOSE QUASAR PAIRS

Kate H. R. Rubin[1,2], Joseph F. Hennawi[2], J. Xavier Prochaska[2,3],
Robert A. Simcoe[4], Adam Myers[5], and Marie Wingyee Lau[3]
[1] Harvard-Smithsonian Center for Astrophysics, 60 Garden Street, Cambridge, MA 02138, USA; krubin@cfa.harvard.edu
[2] Max-Planck-Institut für Astronomie, Königstuhl 17, D-69117 Heidelberg, Germany
[3] Department of Astronomy & Astrophysics, UCO/Lick Observatory, University of California, 1156 High Street, Santa Cruz, CA 95064, USA
[4] MIT-Kavli Institute for Astrophysics and Space Research, Massachusetts Institute of Technology, Cambridge, MA 02139, USA
[5] Department of Physics and Astronomy, University of Wyoming, Laramie, WY 82072, USA
Received 2014 September 24; accepted 2015 May 18; published 2015 July 16

ABSTRACT

We use spectroscopy of close pairs of quasars to study diffuse gas in the circumgalactic medium (CGM) surrounding a sample of 40 damped Lyα systems (DLAs). The primary sightline in each quasar pair probes an intervening DLA in the redshift range $1.6 < z_{\rm DLA} < 3.6$, such that the second quasar sightline then probes Lyα, C II, Si II, and C IV absorption in the CGM transverse to the DLA to projected distances $R_\perp < 300$ kpc. Analysis of the Lyα profiles in these CGM sightlines constrains the covering fraction ($f_{\rm C}$) of optically thick H I (having column density $N_{\rm H\,I} > 10^{17.2}$ cm^{-2}) to be $\gtrsim$30% within $R_\perp < 200$ kpc. Strong Si II λ1526 absorption with equivalent width $W_{1526} > 0.2$ Å occurs with an incidence $f_{\rm C}(W_{1526} > 0.2\ \text{Å}) = 20^{+12}_{-8}$% within $R_\perp < 100$ kpc, indicating that Si II absorption associated with DLAs probes material within a physical distance $R_{\rm 3D} \lesssim 30$ kpc. However, we find that strong C IV λ1548 absorption is ubiquitous in these environments ($f_{\rm C}(W_{1548} > 0.2\ \text{Å}) = 57^{+12}_{-13}$% within $R_\perp < 100$ kpc), and in addition exhibits a high degree of kinematic coherence on scales up to ~175 kpc. We infer that this high-ionization material arises predominantly in large, quiescent structures extending beyond the scale of the DLA host dark matter halos rather than in ongoing galactic winds. The Lyα equivalent width in the DLA-CGM is anticorrelated with $R_\perp$ at >98% confidence, suggesting that DLAs arise close to the centers of their host halos rather than on their outskirts. Finally, the average Lyα, and C II and C IV equivalent widths measured as a function of $R_\perp$ are consistent with those measured around $z \sim 2$ Lyman break galaxies. Assuming that DLAs trace a galaxy population at lower masses and luminosities, this finding implies that the absorption strength of cool circumgalactic material has a weak dependence on dark matter halo mass at $M_{\rm h} \lesssim 10^{12}\,M_\odot$.

Key words: galaxies: halos – galaxies: ISM – quasars: absorption lines

1. INTRODUCTION

Damped Lyα absorbers (DLAs) tracing H I with a column density $N_{\rm H\,I} \geqslant 2 \times 10^{20}$ cm^{-2} have contained most of the neutral gas since $z \sim 5$ (Wolfe et al. 1986; Storrie-Lombardi & Wolfe 2000). The significant decline in the neutral gas mass density between $z \sim 3.5$ and today, concomitant with the buildup of over half the present-day mass in stars (Hopkins & Beacom 2006), suggests that DLAs dominate the reservoir of fuel for star formation over cosmic time (Wolfe et al. 2005).

However, efforts to establish the direct link between DLAs and the sites of active, ongoing star formation have met with only partial success. The shape of the conjugate Lyα emission and absorption profiles observed "down the barrel" toward luminous Lyman break galaxies (LBGs) at $z > 2$ suggests that their galactic disks have H I surface densities exceeding the DLA threshold (Pettini et al. 2002; Shapley et al. 2003; Steidel et al. 2010). On the other hand, many of the observational programs targeting emission from counterpart galaxies close to quasar sightlines probing DLAs have yielded non-detections. To date, these efforts have revealed only ~10 associated galaxies at $z \sim 2$ (e.g., Möller et al. 2004; Fynbo et al. 2010, 2013; Péroux et al. 2011; Bouché et al. 2012; Krogager et al. 2012; Noterdaeme et al. 2012; Jorgenson & Wolfe 2014), the majority of which were selected for study based on their relatively high metallicity (e.g., Möller et al. 2004; Fynbo et al. 2013). These counterparts are typically within $\lesssim 2''$ ($\lesssim$20 kpc) of the background QSO (Krogager et al. 2012), and in cases for which robust photometry is possible have magnitudes $R \sim$ 24–25.5, or ~0.4−1.5L^* (Reddy et al. 2008).

Systems with lower metallicities than those targeted in the aforementioned imaging studies, however, likely trace a much fainter, less massive galaxy population. The tight positive correlation between DLA metallicities and both the kinematic width of unsaturated low-ionization metal absorption and the equivalent width (W) of saturated transitions (i.e., Si II λ1526) is evocative of the mass–metallicity relation established for galaxies from the local universe out to $z \sim 2$ (Tremonti et al. 2004; Erb et al. 2006a; Møller et al. 2013), inspiring the inference that W_{1526} traces the kinematics (and hence the mass) of DLA host dark matter halos (Prochaska et al. 2008; Neeleman et al. 2013). Indeed, searches for individual DLA hosts selected without regard for metallicity have resulted in very few detections, and a recent statistical study of the rest-frame UV flux arising within $\lesssim$10 kpc of DLAs demands that the vast majority of these systems are forming stars at a rate $\leqslant 2\,M_\odot$ yr^{-1} (Fumagalli et al. 2015). Such stringent limits strongly suggest that DLAs must be hosted by low-luminosity (~0.1L^*), low-mass galaxies (see also, e.g., Noterdaeme et al. 2014).

At the same time, however, DLA velocity widths are too large to arise from the rotational motions of individual dwarf systems (>60 km s^{-1}; Prochaska & Wolfe 1997; Wolfe et al. 2005). Studies of DLAs in early cosmological simulations invoked multiple neutral gas "clumps" virialized within a

single dark matter halo to satisfy this latter constraint (e.g., Haehnelt et al. 1998; Nagamine et al. 2004; Pontzen et al. 2008). More recent work has suggested that some fraction of DLAs arise in cold, dense inflowing streams extending over many tens of kiloparsecs and feeding star formation in a massive central galaxy (Razoumov et al. 2008; Fumagalli et al. 2011; Cen 2012), and/or that they trace wind material lofted away from galactic disks by star formation driven outflows (Pontzen et al. 2008; Razoumov et al. 2008). We note, however, that none of these cosmological simulations have been able to match the full DLA velocity width distribution (although see Bird et al. 2015 for recent success along these lines). Moreover, a constraint on the bias of DLAs from measurement of their cross-correlation with Lyα forest absorption implies they must also arise in dark matter halos with masses exceeding $\sim 10^{12}\ M_{\odot}$ (Font-Ribera et al. 2012). As clustering measurements suggest that such massive halos host luminous LBGs at $z \sim 2$ (Adelberger et al. 2005; Conroy et al. 2008; Rakic et al. 2013) with star formation rates (SFR) of ~20–50 $M_{\odot}\ \mathrm{yr}^{-1}$ (Erb et al. 2006b), this finding lies in apparent conflict with the stringent limits imposed on DLA-galaxy UV luminosities by direct imaging studies (Fumagalli et al. 2015). Most recently, study of the distribution of neutral hydrogen around galaxy halos over a broad mass range in hydrodynamical simulations of large cosmological volumes has offered a possible resolution to this tension, predicting that DLAs are most closely associated with very faint galaxies (SFR $<0.1\ M_{\odot}\ \mathrm{yr}^{-1}$) at $z \sim 3$, but that many of them (~40%) still arise within 300 projected kiloparsecs of bright LBGs due to clustering effects (Rahmati & Schaye 2014).

Together, these findings and predictions highlight a number of questions regarding the nature of DLAs. To date, few experiments have assessed the incidence of DLAs as a function of halo mass (Prochaska et al. 2013a; hereafter QPQ6), the spatial extent of DLAs (e.g., Cooke et al. 2010), or the location of these systems within their host halos (e.g., in extended streams or in compact, central galaxy disks). In principle, however, empirical constraints on these quantities can directly relate the cold gas content of DLAs with the star-forming regions they will feed.

One avenue toward meeting this goal is the measurement of the cool hydrogen and metal content in the environments surrounding DLAs, i.e., the study of their circumgalactic medium (CGM). The more diffuse material in these regions must likewise compose the fuel for star formation at later epochs and is likely enriched by the large-scale outflows driven by current and past star formation in nearby galaxies (Heckman et al. 1990; Veilleux et al. 2003, 2005). Studies leveraging spectroscopy of lensed QSOs have recently begun to provide measurements of the CGM close to a small sample of DLAs (~7) over $\lesssim$10 kpc scales (Smette et al. 1995; Lopez et al. 2005; Monier et al. 2009; Cooke et al. 2010), with the vast majority of these systems manifest as DLAs toward only one of the QSO images. Adopting a model assuming that the H I column declines exponentially with projected distance, Cooke et al. (2010) found typical scalelengths for $N_{\mathrm{H\,I}}$ of 0.2–2.6 kpc for this sample. Their analysis suggests that such scale lengths imply total DLA sizes of ~10 kpc, supporting a picture in which the neutral material has a highly localized, compact structure. In one of the only studies of the spatial distribution of cool gas absorption around DLAs on scales larger than ~10 kpc, Ellison et al. (2007) reported on spectroscopy of a $z \sim 3$ binary QSO separated by ~100 kpc (also included in the present analysis), identifying a $z = 2.66$ absorption system having $N_{\mathrm{H\,I}} > 10^{20.1}\ \mathrm{cm}^{-2}$ in both QSO sightlines. From comparison with the H I distribution in cosmological "zoom-in" simulations of two $10^{11.8}\ M_{\odot}$ halos (Razoumov & Sommer-Larsen 2006), both of which have DLA-absorbing material distributed on scales $\ll$100 kpc, they concluded that the coincidence is most likely due to a structure hosting more than one massive galaxy.

However, most studies of the $z \sim 2$ CGM to date have focused on the areas surrounding strongly star-forming or active-galactic-nucleus-dominated systems which are identified with relative ease in deep imaging and spectroscopic surveys. LBGs, photometrically selected from deep near-UV and optical imaging as described in Steidel et al. (2003, 2004) and Adelberger et al. (2004), are now known to be surrounded by an envelope of H I which is optically thick (with $N_{\mathrm{H\,I}} > 10^{17.2}\ \mathrm{cm}^{-2}$) in ~30% of sightlines to projected distances of $R_{\perp} < 200$ kpc (Rudie et al. 2012; Crighton et al. 2013, 2014). Several studies taking advantage of a large sample of close pairs of luminous quasars (Hennawi et al. 2006a, 2010) have explored the gaseous environments of $z \sim 2$ quasar-host galaxies, revealing a $\gtrsim$60% incidence of optically thick, metal-enriched material out to $R_{\perp} < 300$ kpc, with enhanced H I absorption extending to even larger scales (>1 Mpc; Hennawi et al. 2006b; Hennawi & Prochaska 2007, 2013; Prochaska et al. 2013b or QPQ5 hereafter; QPQ6). Taken together, these studies demonstrate clear, qualitative differences between the H I and metal absorption properties of material tracing the high-mass dark matter halos hosting high-redshift quasars (with masses $>10^{12.5}\ M_{\odot}$; Wild et al. 2008; White et al. 2012; Font-Ribera et al. 2013) and the gas in halos of more modest masses hosting LBGs ($\sim 10^{11.6-12}\ M_{\odot}$; Adelberger et al. 2005; Conroy et al. 2008; Rakic et al. 2013). Detailed studies of the CGM around $z < 1$ systems suggest a similar trend of increasing H I and low-ionization metal absorption strength with halo mass (Churchill et al. 2013; Bordoloi et al. 2014; Werk et al. 2014; Prochaska et al. 2014 or QPQ7 hereafter), although the strength of this trend varies depending on the internal properties of the central galaxies, particularly at the highest halo masses (Chen et al. 2010; QPQ7). This latter caveat aside, characterization of these quantities in DLA environments offers a point of comparison with magnitude-selected samples, providing the opportunity to differentiate based on the absorption strength kinematics of this CGM material. There has in addition been significant recent progress toward predicting the properties of the CGM using cosmological "zoom-in" simulations (e.g., Fumagalli et al. 2014a; Faucher-Giguère et al. 2014) with a particular focus on developing these predictions over a broad range in halo mass. Study of the diffuse gas surrounding DLAs will assess the degree of metal enrichment due to the effects of stellar feedback acting from nearby star-forming regions, potentially providing the only constraint on feedback physics in the lowest-mass halos studied in these simulations.

Using a subset of the large sample of close pairs of $z \gtrsim 2$ quasars referenced above (Hennawi et al. 2006a, 2010), we have searched each quasar sightline for instances of DLA absorption in the foreground of both of the paired quasars. Here we report our measurements of the Lyα and metal-line absorption strength and kinematics in the CGM out to $R_{\perp} < 300$ kpc around 40 of these systems, obtained from spectroscopy of the secondary quasar in each pair. Our sample

selection and data set are described in Section 2, and our methods for assessing CGM absorption are described in Section 3. We present our results in Section 4, and discuss their implications for the nature of DLAs and their relationship to luminous galaxies in Section 5. We adopt a ΛCDM cosmology with $\Omega_M = 0.26$, $\Omega_\Lambda = 0.74$, and $H_0 = 70\ \mathrm{km\ s^{-1}\ Mpc^{-1}}$ throughout.

2. DATA AND SAMPLE SELECTION

Our DLA sample is drawn from an ongoing survey to obtain medium-resolution spectroscopy of close quasar pairs at $z \gtrsim 2$ (QPQ6). These pairs were initially identified via data mining techniques from SDSS photometry (Bovy et al. 2011, 2012). Pair candidates were then observed with low-resolution spectrographs on a suite of 3.5–6.5 m telescopes at the APO, KPNO, MMTO, and Calar Alto Observatory as described in Hennawi et al. (2006a, 2010) to develop a sample of confirmed QSO pairs having transverse separations <300 kpc and minimum redshifts >1.6. We subsequently obtained deep, medium- and high-resolution spectroscopy of many of these quasars using a range of instruments, including LBT/MODS, Gemini/GMOS, Magellan/MagE, Magellan/MIKE, Keck/ESI and Keck/LRIS. These observations and the data reduction procedures are described in detail in Section 2.2 of QPQ6.

Following the publication of QPQ6 we added observations of three additional pairs to this survey. Two of these pairs were observed with the Magellan Echellette Spectrograph (MagE; Marshall et al. 2008) on the 6.5 m Magellan Clay telescope on the nights of UT 2014 February 1–4. These data were collected with the $0\farcs7$ wide slit, and thus have a spectral resolution $R = 4000$ and a wavelength coverage 3050–10300 Å. A single additional pair was observed with the Echellette Spectrometer and Imager (ESI; Sheinis et al. 2002) on the 10 m Keck II telescope on the night of UT 2014 February 5 with the $0\farcs75$ slit. These data provide a spectral resolution $R = 5000$ and wavelength coverage 4000–10100 Å. We reduced these MagE and ESI data following the same procedures listed in QPQ6, making use of custom software available in the public XIDL software package.[6]

We further supplemented this spectroscopic sample with high-signal-to-noise ratio (S/N) SDSS and BOSS spectra where available (Abazajian et al. 2009; Ahn et al. 2012). In the following analysis, we use the highest spectral resolution data at hand for targets which have been observed with more than one instrument, preferring MIKE, ESI, or MagE data, but selecting LRIS, GMOS, or SDSS/BOSS spectra (in order of preference) when echelle or echellette coverage is not available. Quasar redshifts are calculated as described in QPQ6, and have uncertainties in the range $\delta z_{\rm QSO} \sim 270$–$770$ km s^{-1}.

We performed a by-eye search of each spectrum for the signature of a DLA with Lyα absorption blueward of the Lyα emission line in the foreground quasar in each pair and redward of the Lyman limit at the redshift of the corresponding background quasar. The redshift of each DLA was set by an approximate centroid of the associated low-ionization metal absorption. We fitted a model Voigt profile to the H I absorption in each DLA using custom routines (x_fitdla, also available in the XIDL software package), obtaining $N_{\rm H\,I}$ constraints with typical uncertainties of $\lesssim 0.20$ dex dominated by continuum error and line blending (Prochaska et al. 2003). We then expunged all systems having $N_{\rm H\,I} < 10^{20.1}$ cm^{-2} and lying within $\delta v < 5000$ km s^{-1} of the foreground quasar redshift. This liberal $N_{\rm H\,I}$ limit (slightly lower than the limit defining DLAs, $N_{\rm H\,I} \geqslant 10^{20.3}$ cm^{-2}) increases our sample size while still selecting absorbers which are predominantly neutral (H I/H $\gtrsim 90\%$; Prochaska & Wolfe 1996). Figure 1 shows examples of three of our QSO spectra probing $N_{\rm H\,I} \geqslant 10^{20.1}$ cm^{-2} systems, along with the Voigt profile model fit to each absorber.

Finally, both quasar spectra in every pair probing a DLA were continuum normalized using custom software as described in QPQ6. The average uncertainty in the continuum level resulting from this procedure is ≈5%–10% within the Lyα forest and $\lesssim 5\%$ redward of the QSO Lyα transition (QPQ6). All pairs with CGM sightlines having S/N < 4 Å^{-1} at the wavelength corresponding to the Lyα transition at the DLA redshift (henceforth $\lambda_{\rm obs}^{\rm DLA}$) were then eliminated from the sample. This leaves a total of 40 pairs probing DLAs and with spectral S/N sufficient to constrain the Lyα absorption W in the CGM sightline. For three pairs exhibiting DLAs toward both QSOs, the sightlines were assigned to the DLA and CGM samples arbitrarily and were treated as single systems. The instrumentation, spectral resolution, and date of observation for each of these 40 pairs is listed in Table 1. Representative spectroscopy of the H I and metal-line absorption for three of our sample DLAs (red) and the corresponding CGM sightlines (black) is shown in Figure 2, and spectroscopy of the full sample of 40 pairs is shown in the Appendix. The redshift and H I column density distributions of the sample DLAs are presented in the top and middle panels of Figure 3.

One of the QSO pairs in our sample, SDSSJ1029+2623, with an apparent angular separation $\theta_{\rm obs} = 22\farcs5$, is not a physical pair but rather two images of a lensed QSO at $z = 2.197$. This system was first reported in Inada et al. (2006) and further analyzed by Oguri et al. (2013), who obtained the redshift of the lensing cluster $z_{\rm lens} = 0.584$. We use the relation derived by Cooke et al. (2010) and presented in their Equation (5) to calculate the transverse distance between the two light paths at $z_{\rm DLA} = 1.97830$. This distance, $R_\perp = 7.49$ kpc, is assumed throughout this work, and makes this system the closest QSO "pair" in our sample.

3. LINE PROFILE ANALYSIS

3.1. Equivalent Widths

As a first step in our analysis, we measure the boxcar W of the Lyα absorption at $z_{\rm DLA}$ along the CGM sightline ($W_{\rm Ly\alpha}$). This measurement can be complicated by line-blending with intervening Lyα forest absorbers, particularly for the subset of our sample observed at medium resolution and for systems at $z \gtrsim 2.5$. We search the spectral region within $\delta v \pm 600$ km s^{-1} of $\lambda_{\rm obs}^{\rm DLA}$ by eye to find the "single" H I absorption component closest to $\lambda_{\rm obs}^{\rm DLA}$. We choose the velocity range assigned to each absorber by hand, aiming to encompass the full velocity extent of this single component, and then perform a simple boxcar sum over this velocity range to obtain $W_{\rm Ly\alpha}$. While this method is somewhat subjective, it at least provides a conservative lower bound on the H I absorption strength along the sightline. We additionally record the boxcar W of all absorption within $\delta v \pm 500$ km s^{-1} of $\lambda_{\rm obs}^{\rm DLA}$ in each sightline, $W_{\rm Ly\alpha}^{500}$, placing an upper bound on the H I absorption associated with each system.

[6] www.ucolick.org/~xavier/IDL

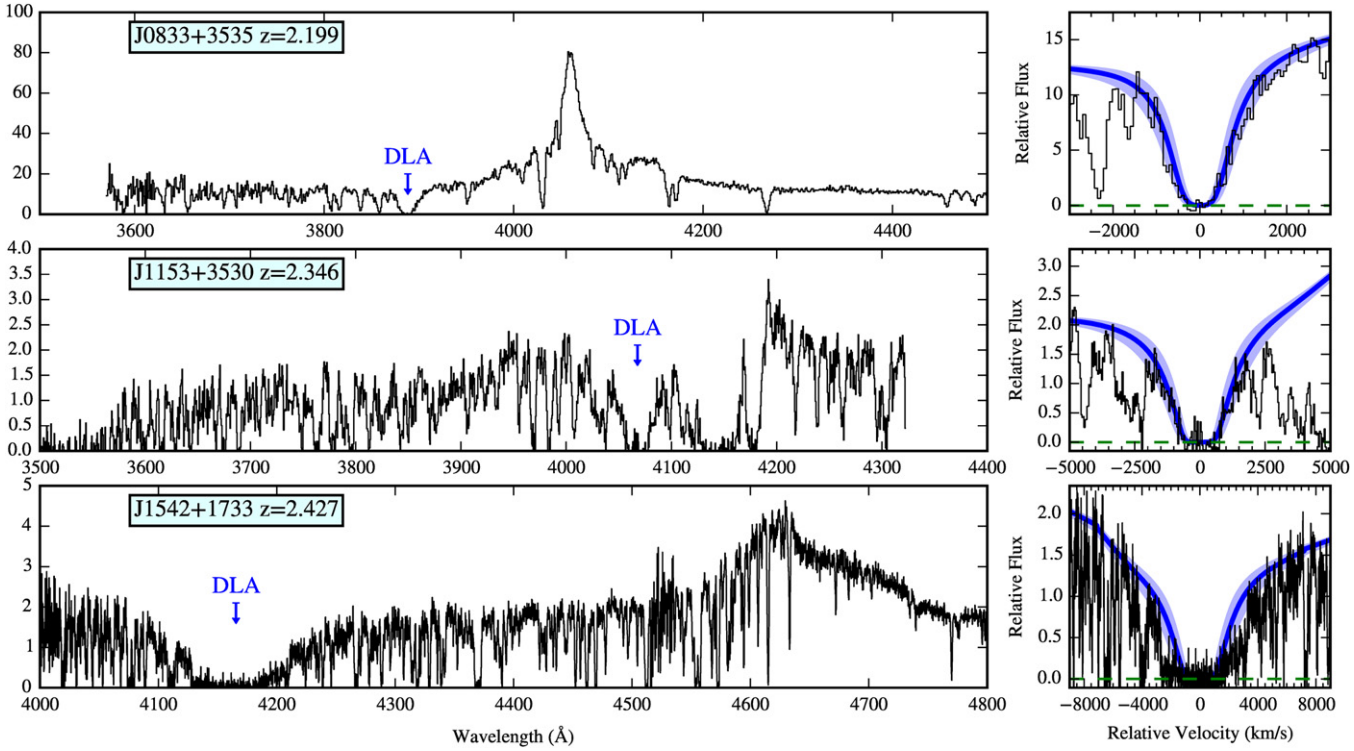

Figure 1. QSO spectroscopy showing three of the DLAs in our sample. The left-hand panels show the entire Lyα forest coverage of each QSO spectrum, with the redshift of the DLA indicated in each panel label and with small blue arrows. The right-hand panels show the Lyα profile of each DLA, with a relative velocity $\delta v = 0$ km s^{-1} corresponding to $z_{\rm DLA}$. The dark blue curves show the best-fit Voigt profile model for each system. The transparent blue area indicates the approximate $\pm 1\sigma$ uncertainty in the fit. These systems span the range in H I column density exhibited by our full DLA sample (from $N_{\rm H\,I} \approx 10^{20.2}$ cm^{-2} in the top panels to $N_{\rm H\,I} \approx 10^{21.1}$ cm^{-2} at bottom).

As we wish to characterize the possible enhancement of Lyα absorption due to the presence of a nearby DLA, we must also assess the "background" strength of Lyα absorption in randomly selected regions of the intergalactic medium (IGM). To do this, we draw from the much larger spectroscopic sample of QSO pairs described in QPQ6, which are similar in both S/N and spectral resolution to the present sample. For each DLA, we select a QSO spectrum at random from all spectra for which $\lambda_{\rm obs}^{\rm DLA}$ is both redward of the Lyβ transition and blueward of the Lyα transition in the rest-frame of the QSO. We also require that $\lambda_{\rm obs}^{\rm DLA}$ does not coincide with Lyα absorption from any close foreground QSO. We do not explicitly require that a given control sightline must have the same S/N and spectral resolution as the corresponding CGM sightline. However, we have verified that the final control sample has a very similar distribution of spectral resolution to that of the CGM sample, and has only a marginally higher median S/N (S/N $\sim$36 Å^{-1} versus S/N $\sim$22 Å^{-1}). We then search the control sightline within a window $\delta v \pm 600$ km s^{-1} around $\lambda_{\rm obs}^{\rm DLA}$, again selecting the strongest H I absorption component closest to $\lambda_{\rm obs}^{\rm DLA}$. This procedure results in a sampling of IGM Lyα absorption with the same redshift distribution as our DLA sample, and which we verified to have a flat distribution of flux-weighted velocity centroids (measured relative to $\lambda_{\rm obs}^{\rm DLA}$). We also measure $W_{\rm Ly\alpha}^{500}$ in these sightlines for comparison with those measured in the DLA-CGM as described above.

The strength of C II 1334, Si IV 1393, Si II 1526, and C IV 1548, 1550 absorption in the CGM sightlines is assessed in a similar manner, although the wavelength range chosen to span each metal-line absorber is limited to fall within the velocity window previously assigned to the corresponding H I absorption. We likewise measure the boxcar W of each of these transitions in the DLAs themselves; here, because such metal-line absorption is nearly always strong and is used to determine $z_{\rm DLA}$, there is no ambiguity in line identification. These measurements, along with $W_{\rm Ly\alpha}$, are listed for each system in Table 2.

3.2. The Average CGM Absorption Strength

We also wish to quantify the average absorption strength of the aforementioned transitions, both to track the change in the mean level of absorption with projected distance from DLAs and to facilitate comparisons with studies of the CGM around systems selected using complementary methods (e.g., QPQ6; Steidel et al. 2010; Crighton et al. 2013, 2014; Turner et al. 2014). To assess this average we coadd the continuum-normalized spectroscopy of our DLA and CGM sightlines covering Lyα, C II, Si IV, Si II, and C IV using the method described in Section 3 of QPQ7. Briefly, we linearly interpolate each spectrum onto 100 km s^{-1} wide pixels, preserving the total normalized flux. We then compute the average flux in each pixel, renormalize the resulting coadd via a linear fit to the pseudo-continuum measured in the velocity windows -4000 km s$^{-1} < \delta v < -3500$ km s^{-1} and 3500 km s$^{-1} < \delta v < 4000$ km s^{-1}, and measure the equivalent width ($\langle W \rangle$) of any resulting features. When generating coadded spectra for the metal-line transitions, we only include sightlines for which the transition of interest lies outside of the Lyα forest (i.e., $\lambda > (1215.6701\ \text{Å})(1 + z_{\rm QSO}) + 20$ Å). For all of the

Table 1
QSO Pair Observations and DLA Sample

Background QSO[a]	Foreground QSO	$z_{b/g}^{QSO}$	$z_{f/g}^{QSO}$	$R_\perp$ (kpc)	z_{DLA}	$N_{H\,I}^{DLA}$ log(cm^{-2})	Instrument	Resolution	Date[b]
J000450.90−084451.9	J000450.65−084449.6	3.00	3.00	35.6	2.75877	20.7	Magellan/MagE	4000	2008 Jun 28
J002802.60−104936.1	J002801.18−104933.9	3.10	2.62	175.6	2.58793	20.9	Keck/ESI	5000	2008 Jul 4
J004003.47+003501.9	J004002.78+003506.5	2.76	2.75	97.5	2.12990	20.6	BOSS	2000	2010 Sep 5
J020143.48+003222.7	J020142.24+003218.4	2.30	2.29	164.7	2.07593	20.1	Gemini/GMOS	1700	2004 Nov 19
J080048.73+354231.3	J080049.89+354249.6	2.07	1.98	202.1	1.78820	20.8	Keck/LRISb	2400	2007 Apr 13
…	…	…	…	…	…	…	SDSS	2000	2001 Nov 25
J083303.32+353559.9	J083302.42+353626.2	2.34	2.34	244.8	2.19860	20.2	BOSS	2000	2010 Dec 2
J091338.97−010704.6	J091338.30−010708.6	2.92	2.75	89.3	2.68874	20.3	Magellan/MagE	4000	2014 Feb 1
J092056.23+131057.4	J092056.00+131102.6	2.43	2.42	54.5	1.60723	20.2	Magellan/MagE	4000	2008 Apr 6
J092056.23+131057.4	J092056.00+131102.6	2.43	2.42	54.0	2.03572	20.1	Magellan/MagE	4000	2008 Apr 6
J093225.60+092500.2	J093226.34+092526.1	2.60	2.42	240.7	2.25198	20.6	Magellan/MagE	4000	2009 Mar 26
J095543.66−012351.5	J095544.29−012357.5	2.84	2.83	91.5	2.72677	20.8	Gemini/GMOS	1700	2013 Sep 2
J101003.46+403754.8	J101001.50+403755.4	2.51	2.18	193.0	2.04454	20.7	BOSS	2000	2011 Jan 9
J102633.21+062909.4	J102633.55+062901.4	3.12	2.89	79.3	2.56408	21.5	Magellan/MagE	4000	2009 Mar 23
J102633.21+062909.4	J102633.55+062901.4	3.12	2.89	77.8	2.78217	20.4	Magellan/MagE	4000	2009 Mar 23
J102913.94+262317.9	J102914.24+262340.1	2.21	2.20	7.5	1.97830	20.5	Keck/LRISb	2400	2007Jan 17
…	…	…	…	…	…	…	Keck/LRISr	3230	2007 Jan 17
…	…	…	…	…	…	…	SDSS	2000	2006 Feb 28
J103900.01+502652.8	J103857.37+502707.9	3.24	3.14	240.9	2.79502	20.2	Keck/ESI	5000	2008 Jan 4
J104506.38+435115.2	J104508.87+435118.2	3.01	2.44	232.3	2.19625	21.2	BOSS	2000	2011 Apr 2
…	…	…	…	…	…	…	Keck/LRISb	2400	2008 May 8
J105644.88−005933.4	J105645.24−005938.1	2.13	2.12	62.7	1.96682	20.3	Magellan/MagE	4000	2014 Feb 1
J111610.68+411814.4	J111611.73+411821.5	3.00	2.94	114.2	2.66270	20.2	Keck/ESI	5000	2006 Mar 4
J115031.14+045353.2	J115031.54+045356.8	2.52	2.52	60.5	2.00063	20.6	Gemini/GMOS	1700	2013 Aug 30
J115302.52+353008.1	J115301.90+353002.9	3.05	2.43	77.5	2.34610	20.7	BOSS	2000	2011 Mar 28
…	…	…	…	…	…	…	Keck/LRISb	2400	2008 May 8
J123635.42+522057.3	J123635.14+522059.0	2.58	2.57	26.1	2.39644	21.1	Gemini/GMOS	1700	2013 Jul 11
J124025.15+432916.5	J124024.93+432914.4	3.26	3.25	25.2	2.97887	21.1	Keck/ESI	5000	2014 Feb 5
J124025.15+432916.5	J124024.93+432914.4	3.26	3.25	24.9	3.09694	20.5	Keck/ESI	5000	2014 Feb 5
J130603.55+615835.2	J130605.19+615823.7	2.17	2.10	142.0	1.88163	20.4	Keck/LRISb	2400	2005 Mar 9
…	…	…	…	…	…	…	SDSS	2000	2002 Feb 20
J130756.18+042215.4	J130756.73+042215.5	3.04	3.01	67.5	2.76528	20.1	Magellan/MIKE	22000	2004 May 9
…	…	…	…	…	…	…	Magellan/MagE	4000	2008 Jun 28
J130756.18+042215.4	J130756.73+042215.5	3.04	3.01	70.3	2.24969	20.1	Magellan/MIKE	22000	2004 May 9
…	…	…	…	…	…	…	Magellan/MagE	4000	2008 Jun 28
J141633.53+351042.6	J141633.04+351057.0	2.92	2.48	134.4	2.08596	20.4	BOSS	2000	2010 Mar 13
J142816.51+023229.2	J142815.67+023243.5	3.02	3.01	158.0	2.62613	21.1	Gemini/GMOS	1700	2013 Sep 2
J152928.37+231415.8	J152929.03+231420.0	2.64	2.49	86.3	2.07736	20.4	BOSS	2000	2011 Apr 29
J154110.40+270231.2	J154110.36+270224.8	3.63	3.62	49.6	3.32992	20.1	Keck/ESI	5000	2011 Apr 29
J154225.81+173322.9	J154226.90+173300.4	3.26	2.78	231.2	2.42660	21.1	Keck/ESI	5000	2008 Jun 5
J155946.27+494326.7	J155947.73+494307.2	1.95	1.86	210.1	1.78449	20.7	Keck/LRISb	2400	2008 May 8
J161302.03+080814.2	J161301.69+080806.0	2.39	2.38	84.4	1.61703	20.5	Magellan/MagE	4000	2008 Jun 29
J162737.24+460609.3	J162738.63+460538.3	4.11	3.82	259.7	3.54960	20.5	Keck/ESI	5000	2007 Apr 11
J163056.72+115250.3	J163055.95+115229.4	3.28	3.26	187.6	3.18047	20.3	Gemini/GMOS	1700	2012 Sep 6
J171946.66+254941.1	J171945.87+254951.2	2.17	2.17	127.3	2.01900	20.8	Gemini/GMOS	1700	2004 Apr 23
J210329.24+064653.3	J210329.37+064649.9	2.57	2.55	32.8	2.13902	20.5	Gemini/GMOS	1700	2013 Jul 11
J214144.49−022946.7	J214144.94−022936.2	2.71	2.70	107.9	2.10624	20.4	Gemini/GMOS	1700	2013 Jul 11
J214620.98−075303.7	J214620.68−075250.6	2.58	2.11	121.3	1.85306	20.5	Keck/LRISb	2400	2007 Aug 17
…	…	…	…	…	…	…	SDSS	2000	2001 Sep 21

Notes.
[a] Object names followed by "…" indicate pairs for which more than one instrument was used.
[b] UT date of the first night this pair was observed by the instrument in column (8).

transitions except C IV, we use a relative velocity window $-500\ \mathrm{km\ s^{-1}} < \delta v < 500\ \mathrm{km\ s^{-1}}$ to measure $\langle W \rangle$. For the latter we choose a window $-500\ \mathrm{km\ s^{-1}} < \delta v < 249\ \mathrm{km\ s^{-1}}$, such that the red edge of the window falls at the midpoint between the two lines in the C IV $\lambda\lambda$1548.195, 1550.770 doublet, and thus avoids absorption from the $\lambda = 1550.770$ Å transition. The uncertainty in this equivalent width is determined by generating 100 bootstrap samples of the spectra, coadding each sample in the same manner, and measuring the dispersion in the resultant mean absorption strength among these 100 samples. The results of the coaddition of all DLA sightlines covering Lyα, C II, Si II, and C IV are shown in Figure 4, along with coadds of the CGM sightlines sorted by $R_\perp$. $\langle W \rangle$ measurements are listed in Table 3 and discussed in Section 4.

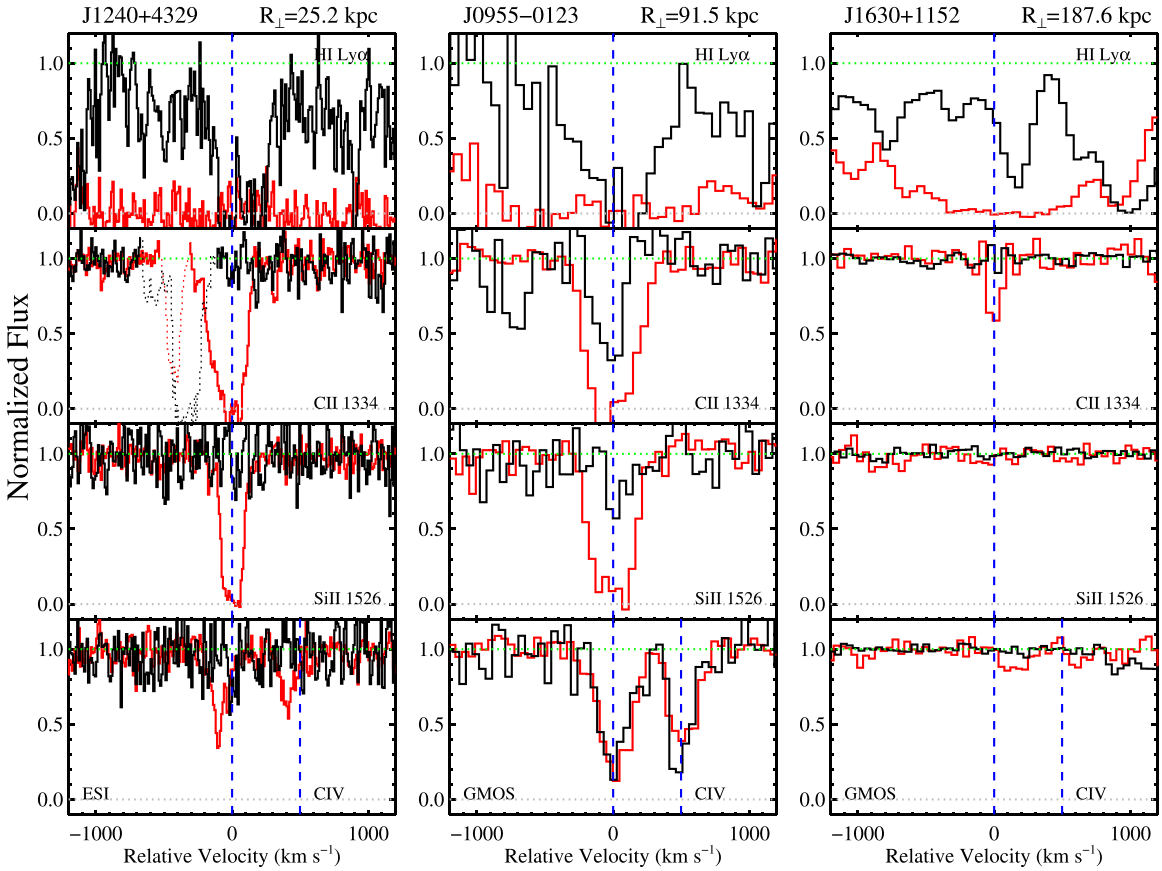

Figure 2. QSO pair spectroscopy representative of our data set. Each column shows the Lyα, C II, Si II, and C IV absorption transitions associated with a DLA (red histogram), with the QSO pair ID and its projected separation indicated above the topmost panel. The blue vertical dashed lines show the rest velocities of the corresponding transitions, with the velocities of both lines in the C IV $\lambda\lambda$1548, 1550 doublet shown in the bottom panels. The black histogram shows the CGM absorption probed by the secondary QSO in each pair at the same redshift as the DLA. The instrument used to obtain each spectrum is indicated in the C IV panels. Absorption due to material unrelated to the system at $z_{\rm DLA}$ is shown with dotted histograms. A subset of our sample was observed at high spectral resolution (FWHM $\lesssim$50 km s^{-1}) with, e.g., Magellan/MagE or Keck/ESI (left-hand column). The majority of our pairs, however, were observed with medium-resolution setups (FWHM $\sim$125–180 km s^{-1}) with Keck/LRIS, Gemini/GMOS, etc. Similar figures showing each of the systems in our sample are provided in Figure 16 the Appendix.

3.3. $N_{H\,I}$ along CGM Sightlines

Finally, we make an effort to assess the column density of H I detected at $\lambda_{\rm obs}^{\rm DLA}$ in each CGM sightline using detailed analysis of the line profile shapes and aided by our W measurements of both H I and metal absorption. A significant fraction of the CGM H I systems in our sample do not exhibit damping wings, and yet have $W_{\rm Ly\alpha}$ values ($\sim$1–2 Å) placing them on the flat part of the curve of growth. In such cases, the line profile shapes depend strongly on gas kinematics rather than gas column, and hence can only be used to place a lower limit on the amount of material along the sightline. However, as we expect these limits to be constraining for galaxy formation models (e.g., Shen et al. 2013; Fumagalli et al. 2014a), we move forward with the following approach (described in complete detail in QPQ6).

For every spectrum with sufficient S/N ($>$9.5 Å^{-1} at $\lambda_{\rm obs}^{\rm DLA}$), we first perform a by-eye Voigt profile fit to the H I line profile using a custom interactive fitting code. This code allows the user to adjust the model Doppler parameter and $N_{\rm H\,I}$ for an optimal fit. In cases for which damping wings are clearly evident ($N_{\rm H\,I} \gtrsim 10^{19.5}$ cm^{-2}), this method provides a relatively tight $N_{\rm H\,I}$ constraint with an uncertainty of $\approx$0.2 dex. For a handful of CGM sightline spectra obtained with MagE or ESI and which are sensitive to optically thin systems with $W_{\rm Ly\alpha}$ $\lesssim$0.5 Å, we may likewise perform a direct comparison with model line profile shapes to obtain a tight column density constraint. For the remaining systems, we use the absence of obvious damping wings to place an upper limit on the gas column by increasing the $N_{\rm H\,I}$ in the model profile until its shape is no longer consistent with the observed line. These measurements and limits are included in Table 2.

The number of absorbers in this latter category is substantial, and we are therefore motivated to search for additional constraints on the gas column. Systems having strong low-ionization metal absorption are very likely optically thick to ionizing radiation (with $N_{\rm H\,I} > 10^{17.2}$ cm^{-2}; Fumagalli et al. 2013) and so we deem any system having low-ionization metal-line (C II 1334 or Si II 1526) $W > 0.3$ Å "optically thick." Systems with particularly high $W_{\rm Ly\alpha}$ values ($>$1.8 Å, corresponding to a single absorber having a Doppler parameter of 40 km s^{-1} and $N_{\rm H\,I} > 10^{18.7}$ cm^{-2}) or which exhibit damping wings are also assumed to be optically thick, even if the corresponding metal absorption is weak, blended with the Lyα forest, or if we lack spectroscopic coverage of the metal transitions of interest. All other saturated systems which lack damping wings, however, are conservatively assumed to have "ambiguous" optical depths (below the previously determined $N_{\rm H\,I}$ limit).

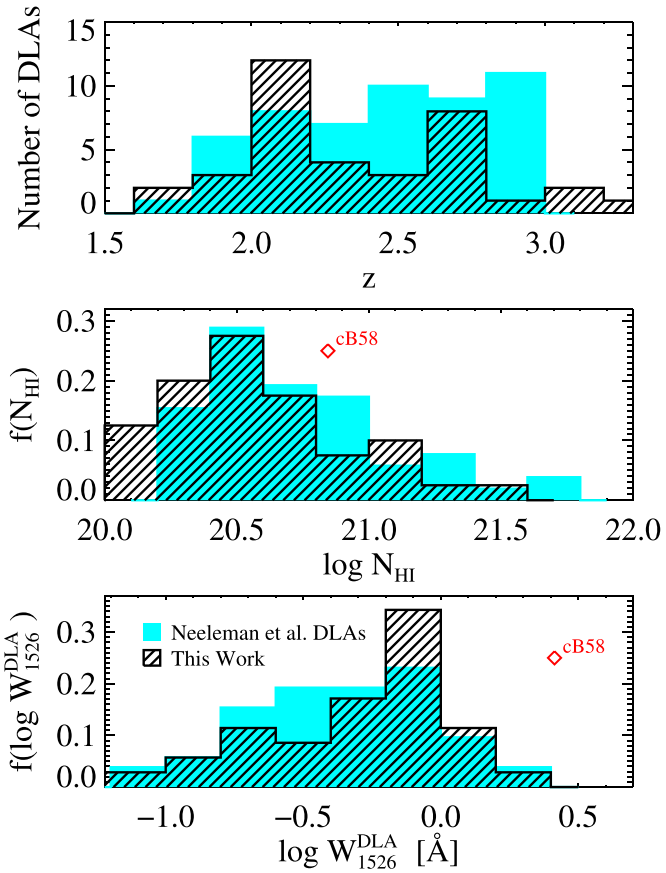

Figure 3. Top: redshift distribution of our DLA sample (black). The redshift distribution of a comparison sample of DLAs drawn from Neeleman et al. (2013) is shown in cyan. The portion of the Neeleman et al. (2013) sample included here falls in the redshift range $1.5 < z < 3.0$ and has spectroscopic coverage of the Si II λ1526 transition. Middle: the distribution of log $N_{\rm H\,I}$ values for our DLA sample (black). The cyan histogram shows the $N_{\rm H\,I}$ distribution for the Neeleman et al. (2013) subsample presented in the top panel. The red diamond marks the $N_{\rm H\,I}$ measured toward the lensed LBG cB58 (Pettini et al. 2002). Bottom: the distribution of log $W_{1526}^{\rm DLA}$ values among the 35 DLAs for which the Si II transition does not fall in the Lyα forest of the corresponding QSO (Section 3.1). For one of these systems, we do not detect significant Si II absorption, but include the DLA in the bin containing the value of our 3σ upper limit on log $W_{1526}^{\rm DLA}$. The cyan histogram and red diamond show the log $W_{1526}^{\rm DLA}$ distribution of the Neeleman et al. (2013) subsample and the logW_{1526} value measured toward cB58 as in the middle panel.

4. RESULTS

4.1. The DLA Sample in Context

In Figure 3 we compare the distribution of redshifts, H I column densities, and Si II λ1526 equivalent widths ($W_{1526}^{\rm DLA}$; bottom panel) of our DLA sample with the distribution of these properties for a random sample of DLAs drawn from the literature (Neeleman et al. 2013; cyan histograms) and selected solely on the basis of their $N_{\rm H\,I}$. The kinematics and metal abundances of this comparison sample have been carefully analyzed in previous work, providing a rich set of ancillary measurements which will aid in later discussion.

The median $z_{\rm DLA}$ of our sample is 2.199, similar to the mean redshift of the sample of LBGs discussed in Rudie et al. (2012) with $\langle z \rangle \sim 2.3$. Furthermore, both the $N_{\rm H\,I}$ and $W_{1526}^{\rm DLA}$ distributions of our DLA sample are similar to those in Neeleman et al. (2013), although our $N_{\rm H\,I}$ distribution extends to slightly lower values due to our liberal DLA selection criterion. The red diamond indicates the W_{1526} and $N_{\rm H\,I}$ measured "down the barrel" in high-resolution spectroscopy of the lensed LBG cB58 (Pettini et al. 2002). The metal-line absorption observed toward the star-forming regions of LBGs has been shown to trace the kinematics of cool gas outflows (e.g., Pettini et al. 2002; Shapley et al. 2003; Steidel et al. 2010), and these outflows may be driving the exceptionally large $W_{1526}^{\rm DLA}$ observed along this unique sightline. On the other hand, Prochaska et al. (2008) and Neeleman et al. (2013) have invoked the tight relationship between DLA metallicity and $W_{1526}^{\rm DLA}$ to suggest that $W_{1526}^{\rm DLA}$ traces the kinematics of a DLA's host dark matter halo, with larger W_{1526} arising in more massive systems. These issues will be discussed further in Sections 5.1.2 and 5.2.2.

4.2. H I Absorption in DLA Environments

Here we present our measurements of the H I absorption strength as a function of projected distance from DLA-host galaxies. The solid black histograms in Figure 5(a) show the distribution of $W_{\rm Ly\alpha}$ in the DLA-CGM, divided into three bins according to $R_\perp$ ($R_\perp < 100$ kpc, 100 kpc $< R_\perp <$ 200 kpc, etc.). The distribution of $W_{\rm Ly\alpha}$ in randomly selected control sightlines, measured as described in Section 3.1, is shown in gray. The CGM $W_{\rm Ly\alpha}$ distributions are skewed to higher equivalent widths relative to the control distributions in every $R_\perp$ bin. A Kolmogorov–Smirnov test indicates a very low probability that the control and CGM distributions are drawn from the same parent population in both the inner ($R_\perp < 100$ kpc; $P = 0.00004$) and middle (100 kpc $< R_\perp <$ 200 kpc; $P = 0.005$) bins. The control and CGM $W_{\rm Ly\alpha}$ distributions in the outermost (200 kpc $< R_\perp <$ 300 kpc) bin, however, are relatively likely to have been drawn from the same parent population ($P = 0.19$).

A comparison of the distributions of $W_{\rm Ly\alpha}^{500}$ in the CGM and control sightlines yields similar results. The median $W_{\rm Ly\alpha}^{500}$ value in the CGM sightlines within $R_\perp < 100$ kpc is 2.2 Å with a dispersion of 0.9 Å, whereas the median and dispersion of $W_{\rm Ly\alpha}^{500}$ values in the control sightlines are 1.0 ± 2.2 Å. A Kolmogorov–Smirnov test indicates a low probability ($P = 0.00004$) that these subsamples are drawn from the same parent population. At 100 kpc $< R_\perp <$ 200 kpc, the $W_{\rm Ly\alpha}^{500}$ values have a median and dispersion of 1.5 ± 1.1 Å and 0.3 ± 2.6 Å in the DLA-CGM and control subsamples, respectively, and are drawn from the same population with a probability $P = 0.07$. At 200 kpc $< R_\perp <$ 300 kpc, however, these $W_{\rm Ly\alpha}^{500}$ distributions are statistically very similar. Taken together, these measurements point to a significant enhancement in Lyα absorption within $R_\perp < 200$ kpc and $\delta v \pm 500$ km s^{-1} of DLAs.

Figure 5(b) again shows our assessment of $W_{\rm Ly\alpha}$ in each CGM sightline, now versus $R_\perp$. The three CGM systems exhibiting exceptionally strong H I absorption (with $N_{\rm H\,I} \geqslant 10^{20.1}$ cm^{-2}) are highlighted in cyan, and are discussed in more detail below. Almost every remaining sightline probes absorption stronger than $W_{\rm Ly\alpha} > 0.6$ Å to nearly $R_\perp \sim 200$ kpc. The two-sided probability that $W_{\rm Ly\alpha}$ is uncorrelated with $R_\perp$ assessed using Kendall's τ rank correlation test is $P = 0.01$ with $\tau = -0.27$, bolstering our conclusion that Lyα absorption

Table 2
DLA and CGM Absorption Line Measurements

QSO Pair Name	$R_\perp$ (kpc)	$z_{\rm DLA}$	$W_{1334}^{\rm DLA}$ (Å)	$W_{1526}^{\rm DLA}$ (Å)	$W_{1548}^{\rm DLA}$ (Å)	$N_{\rm H\,I}^{\rm CGM,a}$ log(cm^{-2})	$W_{\rm Ly\alpha}^{\rm CGM}$ (Å)	$W_{1334}^{\rm CGM}$ (Å)	$W_{1526}^{\rm CGM}$ (Å)	$W_{1548}^{\rm CGM}$ (Å)
J0004–0844	35.6	2.75877	0.564 ± 0.037	0.656 ± 0.055	0.715 ± 0.052	⋯	2.564 ± 0.229	0.011 ± 0.130	0.142 ± 0.084	0.324 ± 0.121
J0028–1049	175.6	2.58793	⋯	0.199 ± 0.020	1.009 ± 0.023	⋯	0.688 ± 0.096	–0.063 ± 0.085	–0.065 ± 0.045	0.433 ± 0.041
J0040+0035	97.5	2.12990	⋯	0.333 ± 0.027	0.919 ± 0.037	⋯	1.855 ± 0.436	⋯	–0.171 ± 0.243	0.420 ± 0.223
J0201+0032	164.7	2.07593	0.616 ± 0.028	0.235 ± 0.026	0.375 ± 0.025	<19.3[c]	2.670 ± 0.055	0.118 ± 0.009	0.053 ± 0.013	0.405 ± 0.013
J0800+3542	202.1	1.78820	0.918 ± 0.013	0.754 ± 0.165	0.984 ± 0.164	<17.2	0.600 ± 0.046	⋯	⋯	⋯
J0833+3535	244.8	2.19860	2.017 ± 0.069	1.258 ± 0.065	2.081 ± 0.063	⋯	0.633 ± 0.315	0.312 ± 0.220	–0.062 ± 0.241	0.092 ± 0.190
J0913–0107	89.3	2.68874	1.272 ± 0.033	0.788 ± 0.028	0.299 ± 0.031	<18.7	1.287 ± 0.033	–0.062 ± 0.058	0.011 ± 0.026	0.136 ± 0.025
J0920+1311	54.5	1.60723	⋯	⋯	⋯	⋯	1.132 ± 0.158	⋯	⋯	⋯
J0920+1311	54.0	2.03572	⋯	0.049 ± 0.014	0.219 ± 0.009	<18.0	0.854 ± 0.027	⋯	0.003 ± 0.015	–0.008 ± 0.011
J0932+0925	240.7	2.25198	0.652 ± 0.049	0.277 ± 0.057	0.265 ± 0.034	<15.0	0.262 ± 0.023	⋯	0.049 ± 0.014[b]	0.007 ± 0.008
J0955–0123	91.5	2.72677	1.957 ± 0.068	1.765 ± 0.065	1.207 ± 0.051	<19.6[c]	2.811 ± 0.192	0.532 ± 0.113	0.373 ± 0.114	1.077 ± 0.113
J1010+4037	193.0	2.04454	⋯	1.511 ± 0.074	1.446 ± 0.064	<18.4	0.897 ± 0.073	0.042 ± 0.051	–0.044 ± 0.055	–0.011 ± 0.051
J1026+0629	79.3	2.56408	⋯	0.896 ± 0.055	2.040 ± 0.064	20.1 ± 0.2[c]	7.783 ± 0.172	2.218 ± 0.034[b]	1.036 ± 0.072	1.896 ± 0.050
J1026+0629	77.8	2.78217	0.785 ± 0.040	0.672 ± 0.052	0.614 ± 0.069	<18.6	1.290 ± 0.109	0.034 ± 0.028	0.144 ± 0.067	0.110 ± 0.067
J1029+2623	7.5	1.97830	⋯	–0.882 ± 0.577	0.019 ± 0.214	<18.7	1.568 ± 0.026	1.421 ± 0.089[b]	–0.034 ± 0.094	–0.121 ± 0.106
J1038+5027	240.9	2.79502	0.227 ± 0.006	0.103 ± 0.007	0.022 ± 0.006[b]	<18.9	1.578 ± 0.037	⋯	0.013 ± 0.019	0.340 ± 0.021
J1045+4351	232.3	2.19625	0.311 ± 0.022	0.177 ± 0.088	0.131 ± 0.141	<19.6	3.057 ± 0.018	⋯	⋯	⋯
J1056–0059	62.7	1.96682	1.150 ± 0.075	1.003 ± 0.062	1.425 ± 0.075	<19.4[c]	3.062 ± 0.102	0.864 ± 0.048	0.726 ± 0.027[b]	2.456 ± 0.046
J1116+4118	114.2	2.66270	0.492 ± 0.009	0.124 ± 0.021	1.136 ± 0.012	20.4 ± 0.2[c]	10.078 ± 0.023	1.004 ± 0.006	0.731 ± 0.016	0.193 ± 0.006
J1150+0453	60.5	2.00063	⋯	0.828 ± 0.044	0.613 ± 0.056	⋯	0.954 ± 0.202	⋯	0.028 ± 0.045	0.114 ± 0.044
J1153+3530	77.5	2.34610	⋯	0.330 ± 0.266	1.035 ± 0.303[b]	<19.4[c]	3.413 ± 0.011	0.411 ± 0.067	–0.028 ± 0.069	0.827 ± 0.068
J1236+5220	26.1	2.39644	0.975 ± 0.060	0.779 ± 0.048	0.462 ± 0.058	<19.1	1.637 ± 0.103	0.173 ± 0.072	0.066 ± 0.044	0.268 ± 0.062
J1240+4329	25.2	2.97887	1.319 ± 0.017	0.997 ± 0.021	0.391 ± 0.019	<19.2	1.924 ± 0.055	0.032 ± 0.022	0.019 ± 0.028	0.088 ± 0.026
J1240+4329	24.9	3.09694	0.879 ± 0.018	0.810 ± 0.018	0.259 ± 0.018	20.1 ± 0.2[c]	5.868 ± 0.108	0.646 ± 0.040	0.231 ± 0.027	0.128 ± 0.028[b]
J1306+6158	142.0	1.88163	⋯	⋯	⋯	<17.2	0.041 ± 0.069	0.019 ± 0.022	1.355 ± 0.390[b]	0.858 ± 0.467
J1307+0422	67.5	2.76528	0.670 ± 0.008	0.536 ± 0.013	0.842 ± 0.016	<18.1	0.766 ± 0.014	–0.005 ± 0.005	–0.006 ± 0.007	0.204 ± 0.007
J1307+0422	70.3	2.24969	⋯	0.220 ± 0.006	0.393 ± 0.006	<18.7	1.140 ± 0.020	⋯	0.057 ± 0.010	0.072 ± 0.012
J1416+3510	134.4	2.08596	⋯	0.606 ± 0.159	0.642 ± 0.129	⋯	2.311 ± 0.200	⋯	⋯	⋯
J1428+0232	158.0	2.62613	⋯	0.740 ± 0.035	0.632 ± 0.028	<19.2	2.015 ± 0.065	⋯	0.079 ± 0.045	0.019 ± 0.036
J1529+2314	86.3	2.07736	⋯	0.630 ± 0.086	0.057 ± 0.096	⋯	0.190 ± 0.224	⋯	0.045 ± 0.142	0.313 ± 0.135
J1541+2702	49.6	3.32992	0.999 ± 0.019	0.546 ± 0.028	1.847 ± 0.034	<19.0	1.779 ± 0.024	0.237 ± 0.017	0.008 ± 0.018	1.398 ± 0.023
J1542+1733	231.2	2.42660	⋯	0.751 ± 0.012	0.160 ± 0.014	<18.5	0.882 ± 0.046	⋯	0.360 ± 0.007[b]	0.019 ± 0.009
J1559+4943	210.1	1.78449	0.173 ± 0.029	⋯	⋯	<17.2	0.281 ± 0.104	0.075 ± 0.044	⋯	⋯
J1613+0808	84.4	1.61703	⋯	⋯	⋯	⋯	1.971 ± 0.139	⋯	⋯	⋯
J1627+4606	259.7	3.54960	⋯	0.032 ± 0.008	0.060 ± 0.009	<14.8	0.324 ± 0.008	–0.003 ± 0.006	0.001 ± 0.006	–0.006 ± 0.007
J1630+1152	187.6	3.18047	0.192 ± 0.073	0.069 ± 0.036	0.161 ± 0.032	<18.6	1.030 ± 0.010	0.002 ± 0.029	0.003 ± 0.018	0.026 ± 0.017
J1719+2549	127.3	2.01900	1.178 ± 0.024	0.694 ± 0.017	0.647 ± 0.013[b]	<17.8	0.854 ± 0.056	–0.029 ± 0.021	–0.003 ± 0.015	0.129 ± 0.020
J2103+0646	32.8	2.13902	⋯	0.429 ± 0.036	0.230 ± 0.040	<19.3	2.231 ± 0.212	⋯	0.298 ± 0.041[b]	0.351 ± 0.046
J2141–0229	107.9	2.10624	⋯	0.468 ± 0.066	0.763 ± 0.064	⋯	1.055 ± 0.310	⋯	0.012 ± 0.087	–0.159 ± 0.082
J2146–0753	121.3	1.85306	⋯	⋯	⋯	<18.8[c]	1.292 ± 0.013	0.418 ± 0.007[b]	0.347 ± 0.082	1.050 ± 0.141

Note. Transitions that fall in the Lyα forest of the corresponding QSO are indicated with "⋯."

[a] $N_{\rm H\,I}$ in the CGM sightline. Values are not listed for spectra that have insufficient S/N to constrain $N_{\rm H\,I}$ (S/N <9.5 Å^{-1} at $\lambda_{\rm obs}^{\rm DLA}$).[b] Transitions which are affected by blending with unassociated systems.[c] H I absorption in the CGM which is optically thick in the Lyman limit (Section 3.3).

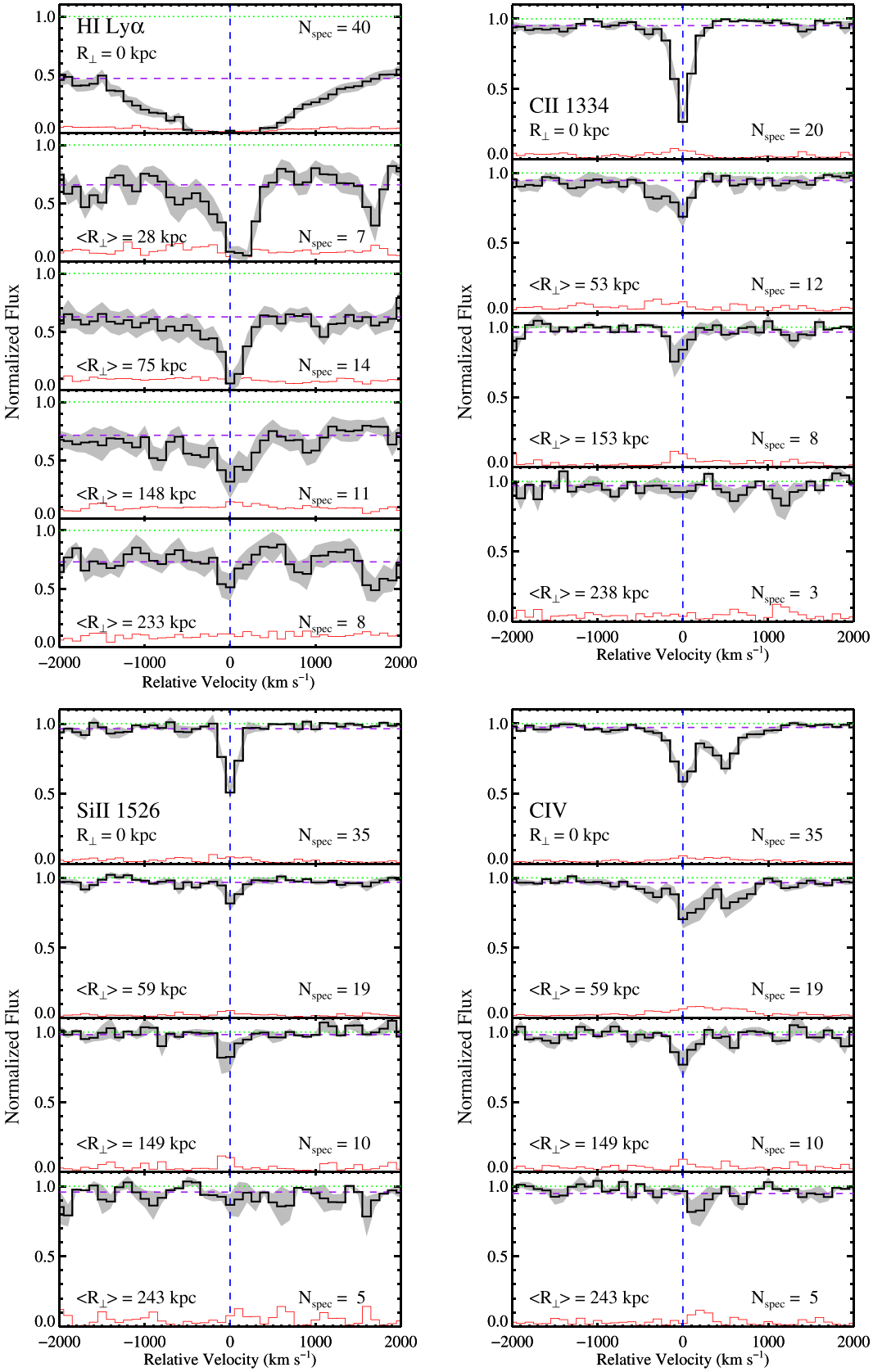

Figure 4. Coadded spectra (black) of our DLA and CGM sightlines covering Lyα (upper left), C II 1334 (upper right), Si II 1526 (lower left), and C IV 1548, 1550 (lower right). The top panels for each transition show the coadds of our full sample of DLA spectra (at $R_\perp = 0$ kpc), while the lower panels show coadds of CGM spectra divided into bins of increasing $R_\perp$ (with the average $R_\perp$ in each bin indicated at the lower left). The number of spectra included in each coadd is indicated at the lower right. The filled gray curves show the $\pm$34th-percentile interval for the flux values in our bootstrap sample in each pixel. The red histogram shows this same 1σ error array. The dashed purple curve shows a linear fit to the pseudo-continuum measured in the windows -4000 km s$^{-1} < \delta v < -3500$ km s^{-1} and 3500 km s$^{-1} < \delta v < 4000$ km s^{-1}.

Table 3
$\langle W \rangle$ Measured in Coadded DLA and CGM Sightlines

$R_\perp$ Range	H I Lyα		C II 1334		Si IV 1393		Si II 1526		C IV 1548	
(kpc)	$\langle R_\perp \rangle$ (kpc)	$\langle W_{\rm Ly\alpha} \rangle$ (Å)	$\langle R_\perp \rangle$ (kpc)	$\langle W_{1334} \rangle$ (Å)	$\langle R_\perp \rangle$ (kpc)	$\langle W_{1393} \rangle$ (Å)	$\langle R_\perp \rangle$ (kpc)	$\langle W_{1526} \rangle$ (Å)	$\langle R_\perp \rangle$ (kpc)	$\langle W_{1548} \rangle$ (Å)
DLAs	0	3.69 ± 0.05	0	0.71 ± 0.13	0	0.32 ± 0.06	0	0.35 ± 0.09	0	0.49 ± 0.07
$0 < R_\perp < 50$	28	1.77 ± 0.33	…	…	…	…	…	…	…	…
$50 < R_\perp < 100$	75	1.40 ± 0.30	…	…	…	…	…	…	…	…
$0 < R_\perp < 100$	60	1.53 ± 0.25	53	0.37 ± 0.11	54	0.15 ± 0.12	59	0.12 ± 0.07	59	0.39 ± 0.12
$100 < R_\perp < 200$	148	1.09 ± 0.39	153	0.10 ± 0.13	154	−0.08 ± 0.04	149	0.15 ± 0.12	149	0.22 ± 0.11
$200 < R_\perp < 300$	233	0.15 ± 0.23	238	0.03 ± 0.05	238	0.04 ± 0.06	243	0.10 ± 0.12	243	0.08 ± 0.05
$0 < R_\perp < 300$	119	1.10 ± 0.18	112	0.23 ± 0.08	117	0.06 ± 0.07	112	0.12 ± 0.06	112	0.30 ± 0.07

Notes. All $\langle W \rangle$ values are measured in a relative velocity window of -500 km s^{-1} $< \delta v <$ 500 km s^{-1}, with the exception of $\langle W_{1548} \rangle$, which is measured in a window of -500 km s^{-1} $< \delta v <$ 249 km s^{-1}. We have excluded spectra from these coadds for which the transition of interest lies in the Lyα forest; i.e., if $\lambda <$ (1215.6701 Å)*$(1 + z_{\rm QSO}) + 20$ Å.

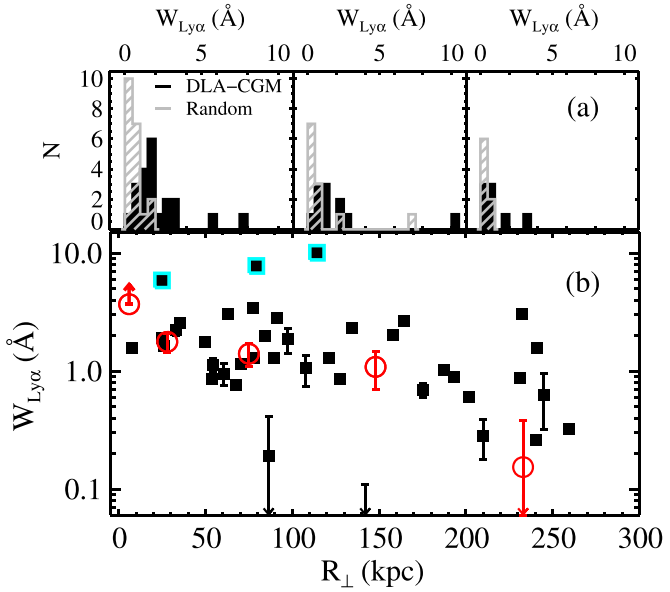

Figure 5. (a) Distribution of $W_{\rm Ly\alpha}$ measured along CGM sightlines (filled black histograms) at 0 kpc $< R_\perp <$ 100 kpc (left), 100 kpc $< R_\perp <$ 200 kpc (middle), and 200 kpc $< R_\perp <$ 300 kpc (right). The gray histograms show the distribution of $W_{\rm Ly\alpha}$ measured in a randomly selected sample of QSO spectra. The distribution of redshifts at which these "control" $W_{\rm Ly\alpha}$ values are measured matches that of the DLA sample in each panel. (b) $W_{\rm Ly\alpha}$ measured along CGM sightlines as a function of projected separation ($R_\perp$) from DLAs. Downward arrows indicate $W_{\rm Ly\alpha}$ values or 1σ-uncertainty intervals which lie below the range of the y-axis. Points outlined in cyan indicate CGM sightlines with $N_{\rm H\,I} \geqslant 10^{20.1}$ cm^{-2}. Red open circles show $\langle W_{\rm Ly\alpha} \rangle$ measured in coadded spectra of DLA sightlines (near $R_\perp = 0$ kpc) and of CGM sightlines divided into four bins in $R_\perp$.

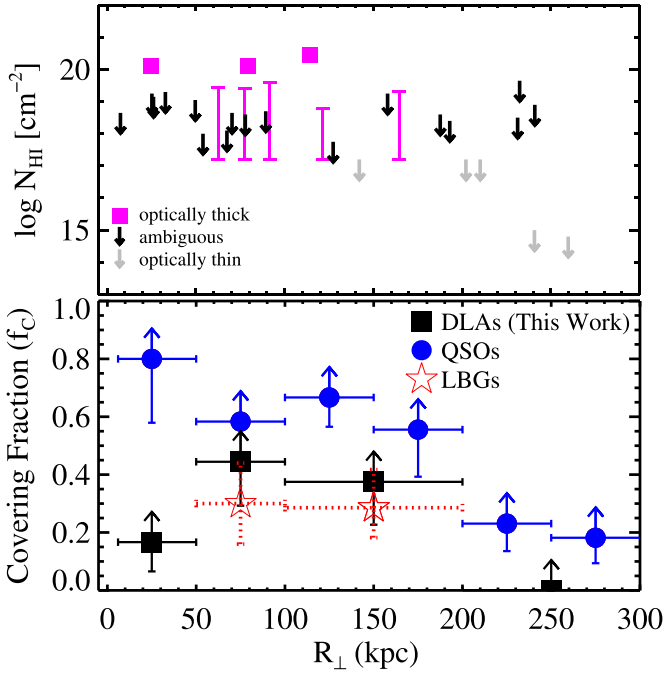

Figure 6. Top: constraints on log $N_{\rm H\,I}$ along CGM sightlines vs. $R_\perp$. Direct measurements of $N_{\rm H\,I}$ from Voigt-profile fitting to damping wings are shown with filled magenta squares. Systems deemed optically thick ($N_{\rm H\,I} > 10^{17.2}$ cm^{-2}) and for which our Voigt-profile fitting yields upper limits on $N_{\rm H\,I}$ are shown with magenta vertical bars. Black arrows show our upper limits on $N_{\rm H\,I}$ for "ambiguous" systems, and gray arrows show upper limits for optically thin systems. Bottom: limits on the covering fraction of optically thick H I measured in several CGM sightline subsamples divided by $R_\perp$ (black). The $R_\perp$ range for each subsample is indicated with horizontal error bars. Vertical error bars show the lower 34th percentile Wilson score confidence intervals. The covering fractions of optically thick material measured around QSO host galaxies (QPQ5) and around LBGs (Rudie et al. 2012) are shown in blue and red, respectively.

close to DLAs is elevated significantly above the level in the ambient IGM.[7] The open red circles show our measurements of $\langle W_{\rm Ly\alpha} \rangle$ as described in Section 3.2, and are similarly indicative of strong absorption extending to ∼200 kpc. We note that these values lie slightly below the $W_{\rm Ly\alpha}$ measurements because we have renormalized our coadded spectra to the level of the pseudo-continuum prior to performing our boxcar $\langle W_{\rm Ly\alpha} \rangle$ measurement. A Kendall's τ rank correlation test of the two-sided probability that $\langle W_{\rm Ly\alpha} \rangle$ is uncorrelated with $R_\perp$ yields $P = 0.04$, demonstrating that the apparent decline in $\langle W_{\rm Ly\alpha} \rangle$ with $R_\perp$ is statistically significant (i.e., we reject a lack of correlation in favor of an anticorrelation with 98% confidence). We also include $\langle W_{\rm Ly\alpha} \rangle$ measured in the coadd of all DLA sightlines at $R_\perp = 6$ kpc in this panel. The method we use to assess the continuum level in coadded spectra underestimates

[7] A Kendall's τ rank correlation test of the probability that $W_{\rm Ly\alpha}^{500}$ is uncorrelated with $R_\perp$ yields very similar results: a two-sided $P = 0.02$ with $\tau = -0.27$.

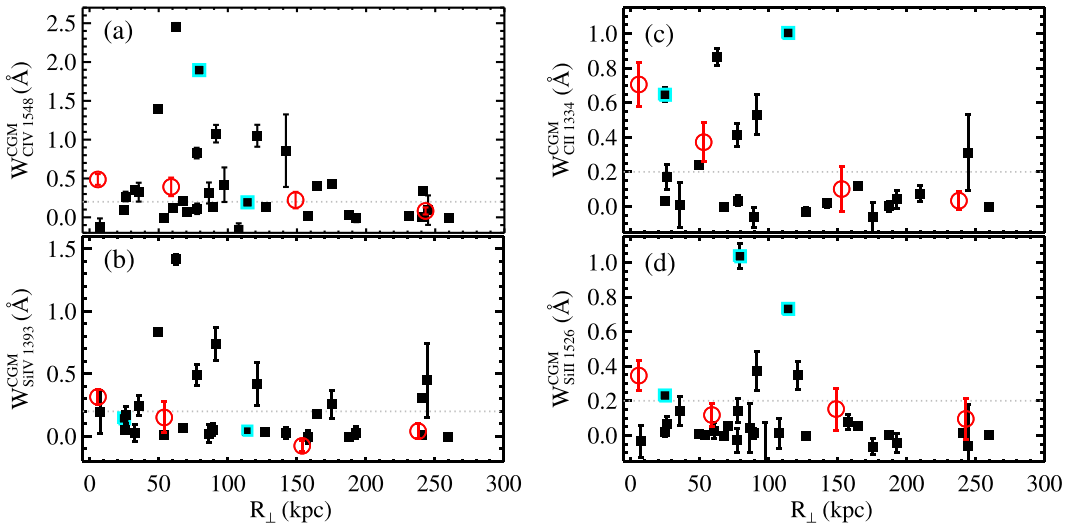

Figure 7. W^{CGM}_{1548} (a), W^{CGM}_{1393} (b), W^{CGM}_{1334} (c), and W^{CGM}_{1526} (d) vs. $R_\perp$ measured in the CGM around DLAs (filled black squares). Points outlined in cyan indicate CGM sightlines with $N_{\rm H\,I} \geqslant 10^{20.1}$ cm^{-2}. Red open circles show $\langle W \rangle$ for the relevant transition measured in coadded DLA sightlines (near $R_\perp = 0$ kpc) and CGM sightlines divided into three subsamples according to $R_\perp$. The horizontal dotted gray line indicates our "strong line" limit of 0.2 Å.

the level of the pseudo-continuum due to ambient IGM absorption in this case, as the Lyα damping wings of DLAs extend well beyond $|\delta v| > 3500$ km s^{-1}. Our value of $\langle W_{\rm Ly\alpha} \rangle$ therefore provides a lower bound on the average Lyα absorption due to the DLAs themselves, and is shown here as a lower limit. When this value is included in the Kendall's τ rank correlation test described above, the probability of no correlation decreases to $P = 0.01$.

Figure 6 (top) shows our constraints on $N_{\rm H\,I}$, with systems having $N_{\rm H\,I} > 10^{17.2}$ cm^{-2} in magenta, with sightlines for which we place an "ambiguous" upper limit on $N_{\rm H\,I}$ in black, and with optically thin sightlines in gray. Most of the CGM sightlines in our sample do not satisfy our DLA $N_{\rm H\,I}$ criterion, consistent with previous findings suggesting that DLAs have a covering fraction $f_C < 1$ for $R_\perp \gtrsim 5$ kpc (Cooke et al. 2010). However, three of these systems (J1026+0629 at $R_\perp =$ 79.3 kpc, J1116+4118 at $R_\perp =$ 114.2 kpc, and J1240+4329 at $R_\perp =$ 24.9 kpc) have CGM $N_{\rm H\,I} \geqslant 10^{20.1}$ cm^{-2} (solid magenta squares). Ellison et al. (2007), reporting on the J1116+4118 system, suggested that this QSO pair probes a relatively overdense environment, and the apparent paucity of such systems in our data set lends further support to this interpretation. Overall, our measurements and limits are indicative of a $\gtrsim$30% incidence of optically thick ($N_{\rm H\,I} > 10^{17.2}$ cm^{-2}) H I out to $R_\perp \sim 200$ kpc. It is only beyond $R_\perp \gtrsim 200$ kpc that we may confidently rule out the presence of optically thick material in a handful of cases.

We estimate a lower limit on the covering fraction of $N_{\rm H\,I} > 10^{17.2}$ cm^{-2} material in several $R_\perp$ bins by dividing the number of bona fide optically thick systems by the total number of sightlines in each bin. These estimates are shown with black squares in Figure 6 (bottom), with the horizontal error bars indicating the bin widths. The vertical error bars show the lower 34th percentile Wilson score confidence intervals. We measure a covering fraction $f_C \sim$ 20%–40% extending to $R_\perp \sim$200 kpc, with our uncertainty intervals indicating f_C is at least $\gtrsim$30% at 50 kpc $< R_\perp <$ 100 kpc. The true covering fraction may be significantly higher than these estimates due to the preponderance of sightlines with "ambiguous" $N_{\rm H\,I}$ constraints within $R_\perp < 200$ kpc; however, f_C cannot be larger than 40 ± 20% at 200 kpc $< R_\perp <$ 300 kpc given the number of optically thin sightlines in our sample at these projected distances.

These measurements are fully consistent with the estimate of the incidence of optically thick H I in the CGM around LBGs from Rudie et al. (2012), shown with red stars in the figure. Measurements of $N_{\rm H\,I}$ in the host halos of luminous QSOs, however, are suggestive of a higher f_C in such environments (QPQ5; blue filled circles). Although our limits on f_C cannot formally rule out consistency with these constraints, the incidence of optically thick systems in the present study and in QPQ5 could be brought into agreement only if it was found that our data set is significantly less complete for optically thick systems than that of QPQ5. Because these data sets are of very similar quality and fidelity, we consider such a discrepancy unlikely.

4.3. Metal-line Absorption in DLA Environments

Figure 7(a) shows our measurement of W_{1548} in each CGM sightline, W^{CGM}_{1548}. For reference, the CGM sightlines having $N_{\rm H\,I} \geqslant 10^{20.1}$cm^{-2} are marked with open cyan squares. We detect very large $W^{CGM}_{1548} > 0.6$ Å to projected distances as large as 121 kpc. However, within this distance there is significant scatter in W^{CGM}_{1548}, with many sightlines exhibiting only $W^{CGM}_{1548} \sim 0.1$ Å. Beyond 150 kpc, we measure W^{CGM}_{1548} as large as ~0.3 Å, but are more likely to find $W^{CGM}_{1548} < 0.2$ Å (see also Figure 8). A Kendall's τ rank correlation test does not rule out a lack of correlation between W^{CGM}_{1548} and $R_\perp$ (yielding a two-sided probability $P = 0.24$), reflecting the overall large scatter in these values at a given $R_\perp$.

The red open circles show $\langle W_{1548} \rangle$ measured in the coadded spectra discussed in Section 3.2, with $\langle W_{1548} \rangle$ in the coadded DLA sightlines marked at $R_\perp = 6$ kpc. The corresponding error bars are determined using our bootstrapping method, and thus reflect both the measurement uncertainty and the scatter in W^{CGM}_{1548} values for each subsample. We find that while $\langle W_{1548} \rangle$ appears to decrease with increasing $R_\perp$, the trend is a weak one:

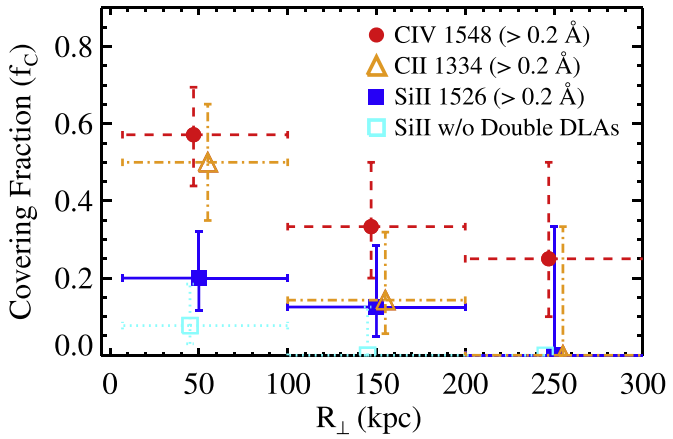

Figure 8. Fraction of CGM systems having $W^{\rm CGM} > 0.2$ Å within three subsamples divided according to $R_\perp$ for Si II 1526 (blue), C II 1334 (orange), and C IV 1548 (red). The $R_\perp$ range for each subsample is shown with horizontal error bars, and the central $R_\perp$ values have been offset slightly for clarity. The vertical error bars indicate the Wilson score 68% confidence intervals. Cyan squares show the covering fraction of $W^{\rm CGM}_{1526} > 0.2$ Å systems after excluding CGM sightlines with $N_{\rm H\,I} \geqslant 10^{20.1}\,{\rm cm}^{-2}$ (that is, excluding "double DLAs").

even the $\langle W_{1548}\rangle$ measured in the DLA sightlines is consistent with $\langle W_{1548}\rangle$ in the CGM at $R_\perp \sim 50$ kpc within the 1σ uncertainty, and the $\langle W_{1548}\rangle$ measured at 100 kpc $< R_\perp <$ 200 kpc differs from the latter by $<2\sigma$. Kendall's τ test for a lack of correlation between $\langle W_{1548}\rangle$ and $R_\perp$ yields a low two-sided probability ($P = 0.04$) only if the value measured in DLA sightlines is included. Without this "down-the-barrel" measurement, the probability is $P = 0.12$, suggestive of a weak anti-correlation of marginal statistical significance.

Figure 7(b) shows our measurements of Si IV 1393 absorption in each CGM sightline ($W^{\rm CGM}_{1393}$). Overall, the absorption strength in this transition is weaker than that of C IV, with nearly all systems exhibiting $W^{\rm CGM}_{1393} < 1$ Å and many having $W^{\rm CGM}_{1393} < 0.2$ Å. Kendall's τ rank correlation test again fails to rule out a lack of correlation between $W^{\rm CGM}_{1393}$ and $R_\perp$, yielding $P = 0.19$. The coadd of CGM sightlines within $R_\perp < 100$ kpc traces a modest $\langle W_{1393}\rangle$ (~0.15 Å), with the coadds of sightlines at $R_\perp > 100$ kpc exhibiting negligible absorption.

Figures 7(c) and (d) show our measurements of CGM absorption in the low-ionization metal transitions C II 1334 ($W^{\rm CGM}_{1334}$) and Si II 1526 ($W^{\rm CGM}_{1526}$). The largest $W^{\rm CGM}$ values in both transitions are ~1 Å, with three of the strongest systems arising in "double" DLAs (having $N^{\rm CGM}_{\rm H\,I} \geqslant 10^{20.1}{\rm cm}^{-2}$). The remaining $W^{\rm CGM}_{1334}$ measurements exhibit a large scatter within 100 kpc, but beyond this are nearly all <0.2 Å. Si II 1526 is the weakest transition explored, with the vast majority (90%) of the 29 CGM sightlines without DLAs yielding weak absorption ($W^{\rm CGM}_{1526} < 0.2$ Å), including the lensed QSO sightline with $R_\perp \sim 7.5$ kpc.

Our measurements of $\langle W_{1334}\rangle$ (red open circles) decline with $R_\perp$, with the DLAs themselves exhibiting an $\langle W_{1334}\rangle$ 2σ higher than $\langle W_{1334}\rangle$ measured at $R_\perp \sim 50$ kpc. Kendall's τ test is suggestive of a weak anti-correlation, both including and without including $\langle W_{1334}\rangle$ measured toward the DLAs ($P = 0.04$ and $P = 0.12$, respectively). $\langle W_{1526}\rangle$, on the other hand, is consistent within the 1σ uncertainty intervals across

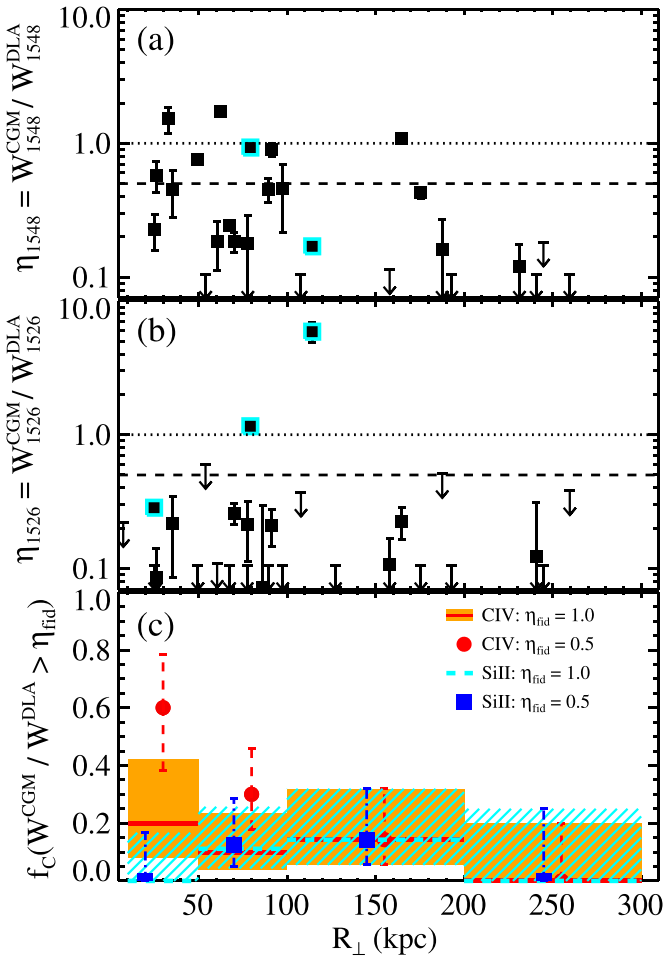

Figure 9. (a) Ratio (η_{1548}) of W_{1548} measured in each CGM sightline ($W^{\rm CGM}_{1548}$) to W_{1548} in the associated DLA ($W^{\rm DLA}_{1548}$), plotted vs. $R_\perp$. Only systems with $W^{\rm DLA}_{1548}$ measurements that are unaffected by line blending are included. Ratios falling below $\eta_{1548} = 0.07$ are indicated with downward arrows placed at $\eta_{1548} \sim 0.1$. Points outlined in cyan indicate CGM sightlines with $N_{\rm H\,I} \geqslant 10^{20.1}{\rm cm}^{-2}$. The horizontal lines are added to guide the eye at ratios of 1.0 and 0.5. (b) Same as panel (a), for Si II ($W^{\rm CGM}_{1526}/W^{\rm DLA}_{1526} = \eta_{1526}$). (c) The fraction of systems having $W^{\rm CGM}/W^{\rm DLA} > \eta_{\rm fid}$ in four subsamples divided by $R_\perp$ for $\eta_{\rm fid} = 1.0$ (solid and dashed horizontal lines) and $\eta_{\rm fid} = 0.5$ (squares and circles). The Wilson score 68% confidence intervals are shown with colored boxes and error bars, respectively. $f_{\rm C}(\eta_{1548} > \eta_{\rm fid})$ values are shown in red and orange, and $f_{\rm C}(\eta_{1526} > \eta_{\rm fid})$ values are shown in blue and cyan. The set of $R_\perp$ ranges adopted for each transition and $\eta_{\rm fid}$ value are the same, and are indicated by the width of the orange/cyan boxes. The plotted points are offset from the centers of these ranges slightly for clarity.

the three CGM subsamples, with $\langle W_{1526}\rangle$ in the coadded DLA sightlines exceeding that in the CGM by only (1.3–2)σ. Here, we find no statistically significant anti-correlation between either $\langle W_{1526}\rangle$ or $W^{\rm CGM}_{1526}$ and $R_\perp$.

We next compute covering fractions for strong metal-line absorption. We consider a system to be "strong" if the equivalent width measurement satisfies $W^{\rm CGM}/\sigma^{\rm CGM}_W > 3$ (where $\sigma^{\rm CGM}_W$ is the uncertainty in $W^{\rm CGM}$) and $W^{\rm CGM} > 0.2$ Å. All systems with securely detected lines (having $W^{\rm CGM}/\sigma^{\rm CGM}_W > 3$) with $W^{\rm CGM}$ below 0.2 Å and all systems having $W^{\rm CGM}/\sigma^{\rm CGM}_W < 3$ with 3σ upper limits on $W^{\rm CGM}$ less than 0.2 Å are treated as sightlines without strong absorption.

We consider constraints from sightlines with 3σ upper limits on $W^{\rm CGM}$ larger than 0.2 Å to be ambiguous in this context, and do not include them in covering fraction estimates. As shown in Figure 8, we detect strong (>0.2 Å) C IV absorption in 57^{+12}_{-13}% of our sightlines within 100 kpc of a DLA. Beyond this $R_\perp$, we estimate a lower $f_{\rm C}\,(W^{\rm CGM}_{1548} > 0.2$ Å)~25%–33%, but find that the $f_{\rm C}$ measurements in all $R_\perp$ bins are consistent within their 1σ uncertainties. We measure a similar incidence for strong C II absorption, finding $f_{\rm C}\,(W^{\rm CGM}_{1334} > 0.2$ Å) $= 50 \pm 15$% within 100 kpc, and estimating $f_{\rm C}\,(W^{\rm CGM}_{1334} > 0.2$ Å) values at larger $R_\perp$ consistent with our constraints on $f_{\rm C}\,(W^{\rm CGM}_{1548} > 0.2$ Å). We also report for completeness that strong Si IV 1393 absorption within 100 kpc of DLAs likewise occurs with a frequency $f_{\rm C}\,(W^{\rm CGM}_{1393} > 0.2) = 0.43^{+0.13}_{-0.12}$, whereas at larger impact parameters 100 kpc $< R_\perp <$ 300 kpc, we measure only $f_{\rm C}\,(W^{\rm CGM}_{1393} > 0.2) = 0.10^{+0.13}_{-0.06}$. Finally, we find $f_{\rm C}\,(W^{\rm CGM}_{1526} > 0.2$ Å) $= 20^{+12}_{-8}$% within 100 kpc, an incidence 2.1σ lower than that measured for C IV and 1.6σ lower than our estimate of $f_{\rm C}\,(W^{\rm CGM}_{1334} > 0.2$ Å). Moreover, the $f_{\rm C}\,(W^{\rm CGM}_{1334} > 0.2$ Å) and $f_{\rm C}\,(W^{\rm CGM}_{1526} > 0.2$ Å) values are respectively slightly higher and lower than, but are both statistically consistent with our measurement of a ~30%–40% incidence of optically thick H I described in Section 4.2. We additionally note that if "double DLA" systems are excluded, the estimated covering fraction of Si II-absorbing material within 100 kpc falls below 10% ($f_{\rm C}\,(W^{\rm CGM}_{1526} > 0.2$ Å) ~ 8%, from 1 strong system among 13 total sightlines).

In Figure 9, we compare our measurements of the CGM metal-line absorption strength with the strength of metal absorption measured along the associated DLA sightline. Here we focus on C IV and Si II, as these transitions exhibit the strongest and weakest CGM absorption, respectively, and also likely trace material in the highest and lowest states of ionization of all of the metal lines included in our analysis (see Section 5.1.2). Panel (a) shows the ratio of W_{1548} measured in the CGM, $W^{\rm CGM}_{1548}$, to that measured in the DLA, $W^{\rm DLA}_{1548}$, as a function of sightline separation. Only systems with unblended coverage of the C IV transition along the DLA sightline are included here: of the 33 systems shown in Figure 7(a), 28 meet this criterion. In cases for which the ratio is <0.07, a symbol is shown either at the 2σ upper limit on the ratio, or at ~0.1 if the upper limit is below the range of the *y*-axis. Double DLA systems are highlighted with cyan open squares. Particularly within $R_\perp <$ 100 kpc, $W^{\rm CGM}_{1548}$ is frequently at least half as large as $W^{\rm DLA}_{1548}$. This finding is quantified in panel *(c)*, in which we show the fraction of pairs ($f_{\rm C}$) exhibiting $W^{\rm CGM}_{1548}/W^{\rm DLA}_{1548} = \eta_{1548}$ larger than a fiducial ratio, $\eta_{\rm fid}$, calculated by dividing the number of pairs satisfying $\eta_{1548} > \eta_{\rm fid}$ by the total number of pairs in a given range in $R_\perp$. We choose values of $\eta_{\rm fid} = 1$ (horizontal red bars with confidence intervals in orange) and $\eta_{\rm fid} = 0.5$ (filled red circles). Note that the $R_\perp$ ranges adopted for each value of $\eta_{\rm fid}$ are the same, and are indicated by the width of the horizontal red/orange bars. Sightlines at $R_\perp$~7–50 kpc have a ~20% probability of exhibiting $W^{\rm CGM}_{1548}$ as high as that measured in the associated DLA, and have a ~60% probability of exhibiting $W^{\rm CGM}_{1548}$ which is at least half as strong as $W^{\rm DLA}_{1548}$. The incidence of similarly high *W* ratios decreases at $R_\perp$~50–100 kpc but remains significant ($f_{\rm C}\,(W^{\rm CGM}_{1548}/W^{\rm DLA}_{1548} > 0.5) \sim 30\%$). These results imply that the bulk of the C IV equivalent width observed "down the barrel" along DLA sightlines traces the motions of gas extending well beyond the cold neutral material giving rise to the H I absorption in the systems. This high-ionization absorption may instead be tracing halo gas kinematics dominated by virial motions and/or galactic winds out to distances $\gtrsim$50 kpc. This scenario was first suggested by the finding that the velocity structure of unsaturated, low-ionization metal absorption (tracing neutral material) differs significantly from the velocity structure of C IV in DLAs (Wolfe & Prochaska 2000). Our measurements offer the first direct constraints on the three-dimensional geometry of this high-ionization absorption.

Figure 9(b) shows the same *W* ratios for the Si II transition. Here, it is unusual for $W^{\rm CGM}_{1526}/W^{\rm DLA}_{1526}$ to exceed $\eta_{1526} = 0.5$: if "double DLAs" are excluded, *no* CGM sightlines exhibit a Si II equivalent width greater than that measured toward the associated DLA. Overall, Figure 9(c) demonstrates that only ~10%–15% of sightlines at 50 kpc $< R_\perp <$ 200 kpc exhibit $W^{\rm CGM}_{1526}/W^{\rm DLA}_{1526} > 0.5$. Thus, while Si II absorption in DLAs appears to arise predominantly from gas within $\lesssim$10 kpc of the neutral material, there is a sub-dominant contribution from a gaseous component extending over >100 kpc scales. Inspection of the W_{1334} measurements presented in Table 2 reveals that the situation is similar for C II: of the 16 pairs for which our C II 1334 coverage is unaffected by blending in both sightlines, $W^{\rm CGM}_{1334}/W^{\rm DLA}_{1334} > 0.5$ in only three pairs, and two of these systems are double DLAs. As with Si II, no CGM sightlines which are not also DLAs exhibit $W^{\rm CGM}_{1334}$ larger than $W^{\rm DLA}_{1334}$, and the fraction of sightlines at $R_\perp <$ 200 kpc exhibiting $W^{\rm CGM}_{1334}/W^{\rm DLA}_{1334} > 0.5$ is only ~20%. We discuss this point further in the context of previous results (e.g., Prochaska et al. 2008) in Section 5.1.

4.4. C IV Absorption Kinematics in DLA Environments

As discussed in the previous subsection, the strong similarity in the values of $W^{\rm CGM}_{1548}$ and $W^{\rm DLA}_{1548}$, particularly between sightlines separated by $\lesssim$100 kpc, suggests that these quantities are dominated by absorbing gas extending over large distances from the DLA ($R_\perp \sim$ 7–100 kpc). Motivated by the high quality and high spectral resolution of the data available for many of these sightlines, here we perform a more comprehensive comparison of the properties of these line profiles. Figure 10 shows C IV profiles for the 12 systems with $W_{1548}/\sigma_{W_{1548}} > 4$ in both the CGM and DLA sightlines. Eight of these pairs were observed at echellette resolution, such that our spectra reveal the detailed velocity structure of the profiles. The separations of these sightlines range from $R_\perp = 26$ to 176 kpc.

Several points become evident from examination of this figure. First, we remind the reader that the systemic velocity ($z_{\rm DLA}$) is determined from the centroid of the low-ionization metal absorption arising in the DLAs. This velocity is often very similar to the velocity centroid of higher-ionization absorption, although we see that the DLA C IV profile is significantly offset from $z_{\rm DLA}$ (by a few hundred km s^{-1}) in a handful of cases (most notably for J1026+0629). These offsets notwithstanding, the central velocities, velocity widths, and in several pairs the detailed shapes of the DLA and CGM C IV profiles are remarkably similar.

To quantify these similarities, we calculate the flux-weighted wavelength centroid of each profile, $\delta\lambda_{1548} = \sum_i (1 - f_i)\,\lambda_i / \sum_i (1 - f_i)$, where f_i and λ_i are the continuum-normalized flux and wavelength of individual

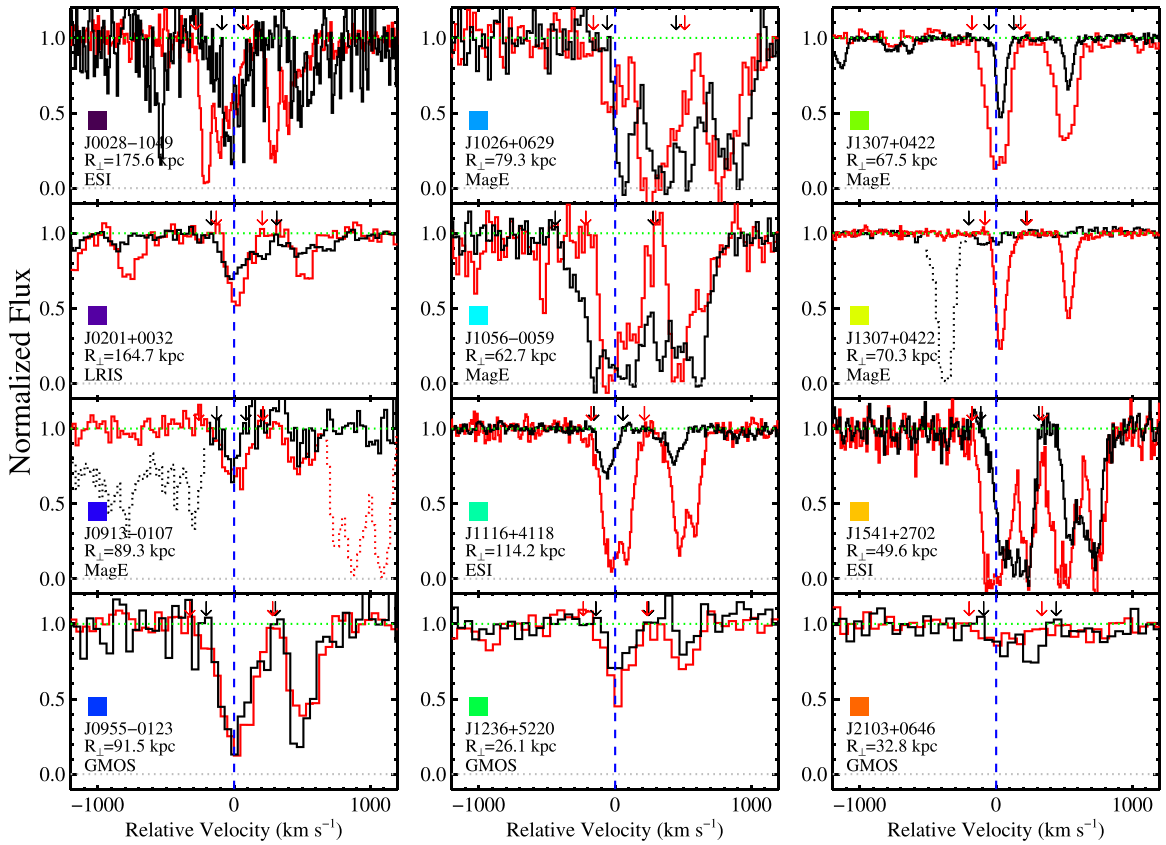

Figure 10. C IV absorption profiles for systems having $W_{1548}/\sigma_{W1548} > 4$ in both the CGM (black) and DLA (red) sightlines. Systems are ordered by the QSO pair ID listed at the bottom of each panel along with the projected separation of the pair and the instrument used to obtain the spectra. The relative velocity is 0 km s^{-1} at z_{DLA} (indicated with a blue vertical dashed line), determined from an approximate centroid of the low-ionization absorption in the DLA sightline. The small black and red downward arrows show the velocity range over which we measure W_{1548}, δv_{1548}, and $\Delta v_{0.75}$ for each system. The large colored squares match each pair to the corresponding points in the left- and right-hand panels of Figure 11. Strong absorption which is physically unrelated to the DLA-CGM systems is shown with dotted histograms.

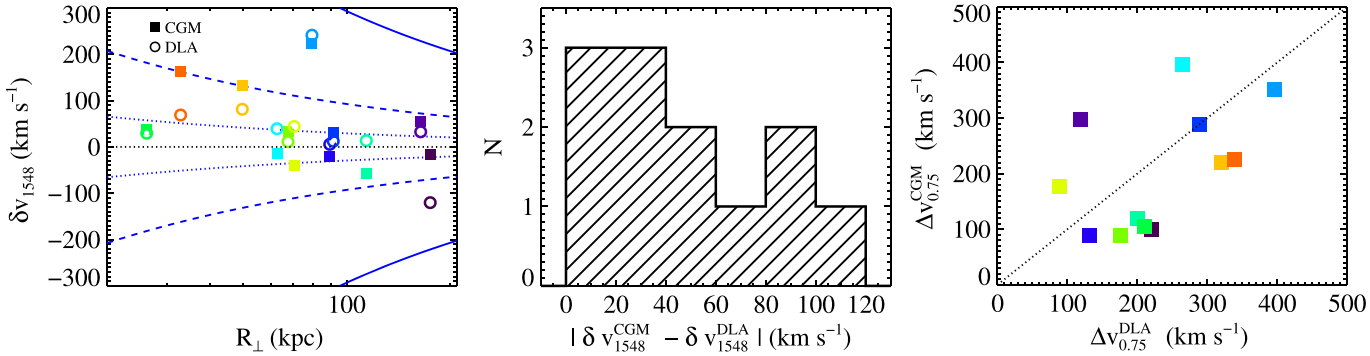

Figure 11. Left: velocity offset between z_{DLA} and the flux-weighted wavelength centroid of C IV absorption (δv_{1548}) in the CGM (solid squares) and DLA (open circles) sightlines in systems for which $W_{1548}/\sigma_{W1548} > 4$. The color of the points marking each pair indicates the corresponding panel in Figure 10. The blue curves show the escape velocity in the radial direction (v_{esc}) as a function of total (not projected) distance from the center of a dark matter halo with mass 10^{10} $M_\odot$ (dotted), 10^{11} $M_\odot$ (dashed), and 10^{12} $M_\odot$ (solid). Middle: the distribution of offsets between δv_{1548}^{CGM} and δv_{1548}^{DLA}. These quantities do not differ by more than 105 km s^{-1} for any pair of sightlines. Right: the velocity range over which C IV absorption expresses 75% of its total W_{1548} ($\Delta v_{0.75}$) in CGM vs. DLA sightlines. The point color indicates the corresponding system in the left-most panel and in Figure 10. The dotted line shows a 1:1 relation. These widths are within 100 km s^{-1} of each other in 7 of 12 cases, and never differ by more than 200 km s^{-1}.

pixels comprising the profile of each system. We show the velocities of these centroids relative to z_{DLA} (δv_{1548}) in Figure 11 (left). Measurements for DLA and CGM sightlines are shown with open circles and filled squares, respectively, and the symbols for each pair are given a unique color to indicate the corresponding profiles in Figure 10. In general, the values of δv_{1548} for the sightlines in each pair are close, and where they are offset from $\delta v_{1548} = 0$ km s^{-1} they are mostly offset in the same sense. We show the distribution of the offsets between δv_{1548}^{CGM} and δv_{1548}^{DLA} in the middle panel of Figure 11. These differences are never larger than 105 km s^{-1}, even for the pairs with the largest sightline separations (up to

$R_\perp = 176$ kpc), and are <60 km s^{-1} for 8 of 12 pairs. We note that a number of these systems have $\delta v_{1548}^{\rm DLA}$ exceeding 100–200 km s^{-1}, such that there is a higher degree of coherence between the C IV absorption covering $\gtrsim$100 kpc scales in these systems than that exhibited by low- and high-ionization absorption along the same QSO sightline. Figure 11 (left) also indicates the radial velocity required for escape from the potential well of dark matter halos over a range of masses ($M_{\rm h} = 10^{10} - 10^{12}\ M_\odot$), or $v_{\rm esc} = \sqrt{2GM_{\rm h}/R}$, with $R = R_\perp$. There are few instances in which the CGM C IV absorption has a central velocity surpassing these values, even for quite low $M_{\rm h} \lesssim 10^{11}\ M_\odot$. However, this material may have an additional component to its velocity vector in the plane of the sky to which our measurements are not sensitive. Furthermore, material with kinematics at the extremes of these quite broad profiles may indeed have the energy to escape from halos with $M_{\rm h} \lesssim 10^{11}\ M_\odot$, even if motions transverse to the line of sight are neglected.

To quantify the velocity width of these profiles, we identify the set of pixels encompassing 75% of the total profile W, defining the central pixel in this set be the pixel whose relative velocity is closest to δv_{1548} (i.e., the flux-weighted C IV 1548 velocity centroid measured as described above). From this set of pixels, we locate those closest to the blue and red profile edges, and calculate the velocity difference between them ($\Delta v_{0.75}$). We compare our measurements of this quantity for each pair of sightlines in the right-most panel of Figure 11. Although there is a large range in the $\Delta v_{0.75}$ values (100–450 km s^{-1}), $\Delta v_{0.75}^{\rm CGM}$ and $\Delta v_{0.75}^{\rm DLA}$ differ by more than 100 km s^{-1} in only 5 of 12 pairs and are weakly correlated (at a $\sim$90% confidence level). Furthermore, $\Delta v_{0.75}$ is almost always larger than the value $|\delta v_{1548}^{\rm CGM} - \delta v_{1548}^{\rm DLA}|$, and exceeds the latter by $>$100 km s^{-1} in six pairs. As anticipated above, the velocities of the pixels at the blue and red edges of these line profiles (identified in the process of estimating $\Delta v_{0.75}$) frequently lie outside of the envelop defined by the halo escape velocity if $M_{\rm h} \lesssim 10^{11}\ M_\odot$.

These comparisons evoke a scenario in which C IV absorption around DLAs arises from gaseous structures having a large velocity dispersion from structure to structure (yielding large velocity widths), but which extend over many tens of kiloparsecs with a high degree of kinematic coherence on these scales. Indeed, such coherence among C IV systems detected along paired QSO sightlines has been noted previously (e.g., Rauch et al. 2001; Martin et al. 2010), but our study is the first to measure this in the vicinity of DLAs. We discuss the implications of these results and their potential to constrain the physical drivers of C IV gas kinematics in Section 5.3.

5. DISCUSSION

5.1. A "Two-dimensional" View of DLAs

5.1.1. The Spatial Extent of DLAs

Much of our understanding of DLAs relies heavily on studies of the absorption along single, pencil-beam sightlines piercing neutral gas in the host galaxy along with any more diffuse material associated with the galaxy's halo in the same beam. However, as noted in Section 1, studies of DLAs toward lensed QSOs (e.g., Cooke et al. 2010) have recently begun to augment these single-sightline analyses, constraining the spatial extent of damped absorption and the coherence of metal-line kinematics over relatively small scales ($\lesssim$10 kpc). Ellison et al. (2007) presented the first exploration of the extent of DLAs over the scales of galaxy halos, identifying a $z = 2.66$ absorption system having $N_{\rm H\,I} > 10^{20.1}$ cm^{-2} in spectroscopy of both sightlines toward the $z \sim 3$ binary QSO J1116+4118 (see also Figure 6, top panel).

The present work adds considerable fidelity to this latter, "two-dimensional" approach to the study of DLAs and their environment. First, the measurements shown in Figure 6 offer direct constraints on the spatial extent of the high column density material giving rise to DLAs on scales larger than $\sim$10 kpc. Of the 30 CGM sightlines in our sample with sufficient S/N to constrain $N_{\rm H\,I}$, only three exhibit $N_{\rm H\,I} \geqslant 10^{20.1}$ cm^{-2}. Within $R_\perp < 120$ kpc (the maximum $R_\perp$ among these double DLA pairs), absorption with $N_{\rm H\,I} \geqslant 10^{20.1}$ cm^{-2} is *absent* from 13 CGM sightlines, most notably from $\sim$75% of sightlines having $R_\perp < 30$ kpc. This is strong confirmation of the conclusion of Cooke et al. (2010) that the physical extent of $N_{\rm H\,I} \geqslant 10^{20.3}$ cm^{-2} absorption in a "typical" DLA must be $<$10 kpc. Taking our measurements at face value, they indicate either (1) that all DLAs have radii $<$10 kpc, with $\sim$10%–20% occurring in overdense environments hosting multiple damped systems, (2) that DLA gas is distributed on scales $>$10 kpc with a low covering factor, or (3) that $\sim$10%–20% of DLAs have physical extents $\gtrsim$30–120 kpc, with all others having much smaller sizes. As we expect these systems to occupy halos having virial radii $\lesssim$100 kpc, the latter scenario would require high-density gas disks to extend over at least 15%–60% of their halo virial diameter (as proposed in, e.g., Maller et al. 2001).

Moreover, we note that the covering fraction of $N_{\rm H\,I} \geqslant 10^{20.1}$ cm^{-2} material within $R_\perp < 100$ kpc of DLAs is $f_{\rm C}^{\rm DLA}(R_\perp < 100\ {\rm kpc}) = 0.13^{+0.11}_{-0.07}$. This measurement may be compared with constraints on the DLA cross section offered by the clustering analysis of Font-Ribera et al. (2012) as follows. The expectation value of the DLA covering fraction within $R_\perp = 100$ kpc measured from a statistical sampling of $N_{\rm H\,I}$ in dark matter halos with masses ranging down to a minimum mass M_0 is

$$\left\langle f_{\rm C}^{\rm DLA} \right\rangle = \frac{\int_{M_0}^{\infty} P(M_{\rm h})\, f_{\rm C}^{\rm DLA}(M_{\rm h};\, R_\perp < 100\ {\rm kpc})\, dM_{\rm h}}{\int_{M_0}^{\infty} P(M_{\rm h}) dM_{\rm h}}. \quad (1)$$

Here, we assume that our experimental setup is sensitive to halos with $M_{\rm h} > M_0$, i.e., that all of these halos host a DLA and hence may fall into our "primary" DLA sample. We further assume that

$$P(M_{\rm h}) = (c/H_0)\Sigma_{\rm DLA}(M_{\rm h}) n(M_{\rm h})$$

describes the typical incidence of DLAs as a function of halo mass $M_{\rm h}$, with $\Sigma_{\rm DLA}(M_{\rm h})$ equal to the DLA cross section (in kpc^2) and $n(M_{\rm h})$ equal to the comoving number density of halos with mass in the interval ($M_{\rm h}$, $M_{\rm h} + dM_{\rm h}$).

If we consider all halos to be isolated such that their DLA cross sections do not overlap on the sky, we can additionally state that the DLA covering fraction measured within

$R_\perp < 100$ kpc for a halo of mass $M_{\rm h}$ is

$$f_{\rm C}^{\rm DLA}\left(M_{\rm h};\, R_\perp < 100\ \ {\rm kpc}\right) = \frac{\Sigma_{\rm DLA}\left(M_{\rm h}\right)}{\pi\,(100\ \ {\rm kpc})^2}.$$

Here we are assuming that the full DLA cross section arises within $R_\perp < 100$ kpc, and that $\Sigma_{\rm DLA}$ cannot exceed $\pi\,(100\ \ {\rm kpc})^2$. The value $\langle f_{\rm C}^{\rm DLA}\rangle$ in Equation (1) is then fully specified given a functional form for $\Sigma_{\rm DLA}(M_{\rm h})$ and a minimum DLA halo mass M_0.

Motivated by trends in the distribution of neutral material over a range in halo masses exhibited in cosmological hydrodynamical simulations, Font-Ribera et al. (2012) explored two parameterizations of $\Sigma_{\rm DLA}(M_{\rm h})$. They first adopted a form

$$\Sigma_{\rm DLA}\left(M_{\rm h}\right) = \Sigma_0\left(M_{\rm h}/M_0\right)^{\alpha}, \tag{2}$$

with Σ_0 a constant. Their estimate of the bias factor of DLAs, in combination with the observed DLA incidence rate, place simultaneous constraints on Σ_0, M_0, and α. For instance, they found that $\alpha = 1$ with $M_0 = 10^{10}\,M_\odot$ requires $\Sigma_{\rm DLA}(10^{12}\ \ M_\odot) = 1400\ \ {\rm kpc}^2$. This particular model yields a low value of $\langle f_{\rm C}^{\rm DLA}\rangle = 0.08$, consistent with our measurement. On the other hand, a model of the form

$$\Sigma_{\rm DLA} = \Sigma_0\left(M_{\rm h}/M_0\right)^2\left(1 + M_{\rm h}/M_0\right)^{\alpha-2} \tag{3}$$

with $\alpha = 1$ and $M_0 = 10^{10}\ \ M_\odot$ satisfies the DLA bias and incidence rate with $\Sigma_{\rm DLA}(10^{12}\,M_\odot) = 2400\ \ {\rm kpc}^2$, but yields a much higher $\langle f_{\rm C}^{\rm DLA}\rangle = 0.26$. This value likewise falls nearly within the $\pm 1\sigma$ uncertainties in our estimate of $f_{\rm C}^{\rm DLA}\,(R_\perp < 100\ \ {\rm kpc})$. Thus, our current constraints on $f_{\rm C}^{\rm DLA}$ are in accord with a large neutral gas cross section (with a characteristic length scale $R_{\rm char} \sim \sqrt{1400\ \ {\rm kpc}/\pi} \sim 20$ kpc) arising in high-mass dark matter halos ($M_{\rm h} \sim 10^{12}\ \ M_\odot$). As noted above, however, given the high incidence of non-detections within $R_\perp < 30$ kpc and in the Cooke et al. (2010) study, this material is most likely distributed with a covering fraction less than unity. Moreover, the factor of >3 variation in $\langle f_{\rm C}^{\rm DLA}\rangle$ between the two models described above suggests that a larger sample of QSO sightlines within $R_\perp < 100$ kpc of DLAs may eventually aid in breaking the degeneracies in these model parameters, further elucidating the relationship between the morphology of DLA absorption and dark matter halo mass.

5.1.2. The Origin of Low-ionization Absorption Associated with DLAs

Among CGM sightlines which do not exhibit a second DLA, we detect optically thick H I within $R_\perp < 100$ kpc with an incidence of ∼23%. We emphasize that we cannot rule out the presence of optically thick material in *any* of the CGM sightlines within this projected distance and that the true incidence of such absorption may be significantly higher. We can, however, place stringent limits on the incidence of low-ionization metal absorption in many of our CGM sightlines. As shown in Figure 7(d), we detect strong Si II with $W_{1526}^{\rm CGM} > 0.2$ Å in only one sightline which does not also probe a DLA (and which has $R_\perp < 100$ kpc), with measurements of $W_{1526}^{\rm CGM}$ falling well below 0.2 Å in the vast majority of the remaining sightlines. The resulting covering fraction for strong Si II absorption in environments outside the high-density neutral material giving rise to DLAs is ∼0.08. Strong absorption from singly ionized carbon is somewhat more prevalent: within $R_\perp < 100$ kpc, of the 10 CGM sightlines with unblended coverage of C II 1334 and which do not probe DLAs themselves, 4 exhibit $W_{1334}^{\rm CGM} > 0.2$ Å. This enhanced incidence may be due in part to an overall higher abundance of carbon relative to silicon, as observed in the solar system ($\log({\rm C/H})_\odot = -3.57$ versus $\log({\rm Si/H})_\odot = -4.49$; Asplund et al. 2009). In addition, the high ionization potential of C II (24.38 eV) allows it to survive in material over a broad range of ionization states, unlike Si II, which has an ionization potential of 16.35 eV and is destroyed as $\log n_\gamma/n_{\rm H}$ increases to $\gtrsim -1.5$ (with n_γ equal to the photon density and $n_{\rm H}$ the total hydrogen number density; Werk et al. 2014).

These findings have implications for the interpretation of low-ionization absorption kinematics and equivalent widths measured "down the barrel" toward DLAs themselves. The relatively high incidence of strong C II absorbers to $R_\perp \lesssim 100$ kpc suggests that the significant C II absorption measured in our DLA sightlines (Figure 4; Table 2) in part traces material extending over scales larger than the neutral material composing the DLAs, and hence may arise in a more highly ionized halo gas component. However, as discussed in Section 4.3, $W_{1334}^{\rm CGM}$ exceeds $0.5W_{1334}^{\rm DLA}$ in only ∼20% of sightlines within 200 kpc, indicating that the C II absorption observed down the barrel predominantly traces material within a few tens of kiloparsecs. Regarding Si II, our low limits on $W_{1526}^{\rm CGM}$ at $R_\perp \sim$ 30–100 kpc indicate that $W_{1526}^{\rm DLA}$ measurements must be dominated by material within a physical distance $R_{\rm 3D} \lesssim 30$ kpc. Furthermore, Figure 9 shows that $W_{1526}^{\rm CGM}$ is nearly always <50% of $W_{1526}^{\rm DLA}$, likewise implying that the Si II gas kinematics are typically driven by gas motions close to the DLA. If the tight correlation between DLA metallicity and $W_{1526}^{\rm DLA}$ (Prochaska et al. 2008; Neeleman et al. 2013) is indeed driven by a galaxy mass–metallicity relation, this suggests that $W_{1526}^{\rm DLA}$ must preferentially trace galaxy dynamics on small scales, analogous to emission-line tracers of H II region kinematics (e.g., Weiner et al. 2006). In contrast to these results, we have found that the kinematics of high-ionization material (e.g., C IV) must arise predominantly from the motions of gas extending over much larger scales. We discuss the processes which may be most relevant to these motions in Section 5.3.

5.2. The DLA-CGM and Magnitude-selected Galaxy Environments

5.2.1. Geometrical Considerations

As one of our primary goals is to understand DLAs in the context of their host dark matter halos and their relation to star formation at high redshift, we wish to draw comparisons between the absorption strength of material in and around DLAs with that around optically selected galaxies at $z \sim 2$. Ideally, we would directly compare the CGM absorption strength as a function of projected distance from the centers (or density peaks) of DLA host halos with that of halos of known mass scale. However, because the precise location of DLAs within their surrounding dark matter distribution is not well understood, we must first consider how our experimental design affects our ability to constrain the projected radial absorption profile of the halos selected via our chosen technique.

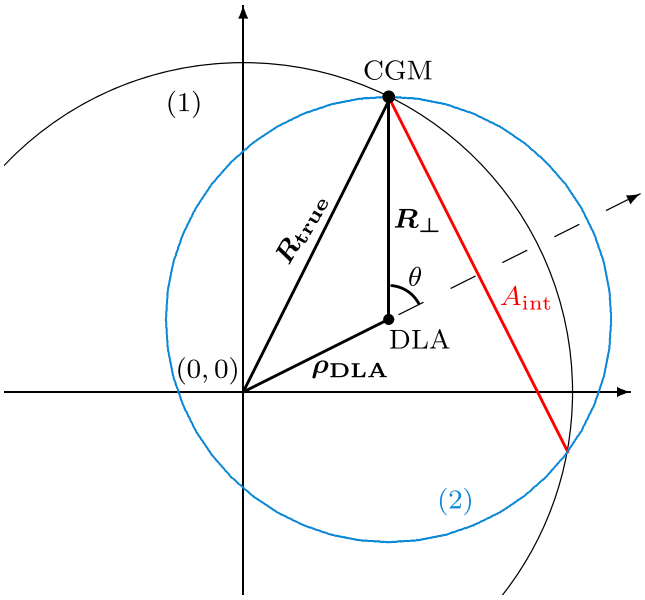

Figure 12. Diagram illustrating our experimental setup. The central density peak of a DLA-selected halo is located at the origin. The DLA lies at the small filled circle at $\boldsymbol{\rho}_{\rm DLA}$. The set of sightlines that may be probed by a secondary QSO at a given $\boldsymbol{R}_\perp$ is indicated with the blue circle (2). One such sightline is marked with a second small filled circle and labeled "CGM." The "true" location of a given sightline along this circle relative to the halo center is indicated by $\boldsymbol{R}_{\rm true}$. We denote the circle centered at the origin with radius $\boldsymbol{R}_{\rm true}$ as circle (1). The chord, $A_{\rm int}$, is defined by the intersection points between circles (1) and (2).

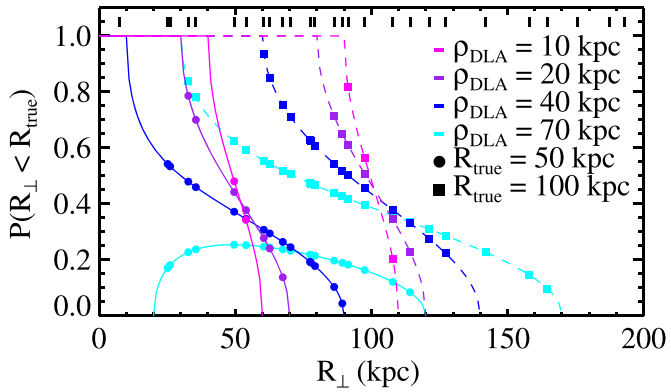

Figure 13. Probability that a sightline at $R_\perp$ falls within a "true" projected distance from the associated halo center ($R_{\rm true}$), $P(R_\perp < R_{\rm true})$, as a function of $R_\perp$ for values of $R_{\rm true} = 50$ kpc (solid curves) and $R_{\rm true} = 100$ kpc (dashed curves). Colors correspond to different values of $\rho_{\rm DLA}$ as indicated in the legend. The set of $R_\perp$ values for the QSO pairs with coverage of C IV in the CGM sightline is shown with black vertical hashes toward the top of the figure. The points show the value of $P(R_\perp < R_{\rm true})$ corresponding to each sightline for $R_{\rm true} = 50$ kpc (circles) and $R_{\rm true} = 100$ kpc (squares), excluding points at $P(R_\perp < R_{\rm true}) = 1$.

As noted in Section 1, in the few cases for which an emission counterpart to a previously known DLA has been recovered, they are typically located within $\lesssim$20 kpc of the QSO sightline (e.g., Péroux et al. 2011; Krogager et al. 2012), suggestive of a scenario in which DLAs arise close to the peak halo density locus. On the other hand, cosmological "zoom-in" simulations predict that DLAs can trace inflowing streams or cool outflows extending to the host halo virial radius (Fumagalli et al. 2011; Bird et al. 2014), leaving open the possibility that a significant portion of the DLA cross section is contributed by systems many tens of kpc from the nearest halo center. In this case, the "true" projected distance ($R_{\rm true}$) from the center of a DLA-selected halo for a given CGM sightline in our sample may likewise be many tens of kiloparsecs larger or smaller than the QSO pair sightline separation ($R_\perp$). In particular, given a projected distance from the halo center for a DLA, $\rho_{\rm DLA}$, $R_{\rm true}$ must fall in the range $R_\perp - \rho_{\rm DLA} \leqslant R_{\rm true} \leqslant R_\perp + \rho_{\rm DLA}$. We present a diagram illustrating this scenario in Figure 12.

To determine the probability distribution of $R_{\rm true}$ within this range of values, we consider a circle with a radius defined by the vector $\boldsymbol{R}_\perp$ and centered on the DLA (circle (2) in Figure 12). The DLA is located at $\boldsymbol{\rho}_{\rm DLA}$, with the origin of the coordinate system defined to be at the halo center. We refer to the angle between the vectors $\boldsymbol{R}_\perp$ and $\boldsymbol{\rho}_{\rm DLA}$ as θ. The vector connecting the origin to the CGM sightline, $\boldsymbol{R}_{\rm true}$, forms the third side of a triangle with $\boldsymbol{R}_\perp$ and $\boldsymbol{\rho}_{\rm DLA}$, and its length may therefore be written $|\boldsymbol{R}_{\rm true}| = R_{\rm true} = (R_\perp^2 + \rho_{\rm DLA}^2 - 2R_\perp \rho_{\rm DLA} \cos\theta)^{1/2}$ (where $|\boldsymbol{R}_\perp| = R_\perp$ and $|\boldsymbol{\rho}_{\rm DLA}| = \rho_{\rm DLA}$).

Under the assumption that there is no preferred direction for $\boldsymbol{R}_\perp$, i.e., that θ has a uniform probability distribution in the range $0 \leqslant \theta \leqslant 2\pi$, we draw θ values at random to estimate the resultant probability distribution for $R_{\rm true}$, $P(R_{\rm true})$. We find that $P(R_{\rm true})$ is sharply peaked toward both $R_\perp - \rho_{\rm DLA}$ and $R_\perp + \rho_{\rm DLA}$, meaning that $R_{\rm true}$ is significantly more likely to have a value close to these extremes than close to $R_\perp$. For example, if $\rho_{\rm DLA} = 20$ kpc and $R_\perp = 100$ kpc, the total probability that $R_{\rm true} < 85$ kpc or $R_{\rm true} > 115$ kpc is 46%, whereas the probability that 95 kpc $< R_{\rm true} <$ 105 kpc is only 16%. The form of this distribution must be considered when interpreting the results presented in Figures 5–9: each sightline shown has a non-negligible probability of probing an $R_{\rm true}$ offset from the indicated $R_\perp$ by an amount $\approx\rho_{\rm DLA}$. If $\rho_{\rm DLA}$ is indeed small ($\lesssim$20 kpc), this offset will be $\lesssim$7% of the x-axis coverage of these figures. If $\rho_{\rm DLA}$ is instead on the order of $\sim$100 kpc, the systematic uncertainty in $R_{\rm true}$ will span much of the $R_\perp$ range shown.

In preparation for comparing $\langle W \rangle$ measured in coadded DLA-CGM sightlines to that measured around magnitude-selected samples, we now calculate the probability of a sightline at $R_\perp$ falling within a projected distance $R_{\rm true}$. Here, we consider the intersection of two circles as shown in Figure 12: (1) one of radius $R_{\rm true}$ and centered at the origin (i.e., the halo center) and (2) one of radius $R_\perp$ and centered at $\boldsymbol{\rho}_{\rm DLA}$. The probability that a sightline at $R_\perp$ falls within $R_{\rm true}$ is then simply the fraction of the circumference of circle (2) which falls within circle (1). This probability can be written:

$$P(R_\perp < R_{\rm true}) = \begin{cases} 1, & \text{if} \quad \rho_{\rm DLA} \leqslant R_{\rm true} - R_\perp \\ 1 - \dfrac{1}{\pi}\sin^{-1}\dfrac{A_{\rm int}}{2R_\perp}, & \text{if} \quad R_{\rm true} - R_\perp < \rho_{\rm DLA} \leqslant \dfrac{\rho_{\rm DLA} + R_{\rm true}^2 - R_\perp^2}{2\rho_{\rm DLA}} \\ \dfrac{1}{\pi}\sin^{-1}\dfrac{A_{\rm int}}{2R_\perp}, & \text{if} \quad \rho_{\rm DLA} > \dfrac{\rho_{\rm DLA} + R_{\rm true}^2 - R_\perp^2}{2\rho_{\rm DLA}}. \end{cases}$$

$A_{\rm int}$ is the length of the chord defined by the intersection points of the two circles. In the context of comparing DLA-CGM

absorption measurements against those measured around magnitude-selected samples to a given $R_{\rm true}$, higher values of $P(R_\perp < R_{\rm true})$ indicate higher probabilities that our DLA-CGM measurements with $R_\perp < R_{\rm true}$ actually fall within this $R_{\rm true}$, and hence that we are more likely to be comparing physically analogous regions.

We show the distribution of $P(R_\perp < R_{\rm true})$ expected for our sample adopting representative values of $\rho_{\rm DLA}$ and $R_{\rm true}$ in Figure 13. The set of $R_\perp$ values for the QSO pairs with coverage of C IV in the CGM sightline is shown with black vertical hashes toward the top of the figure. The colored curves show the probability $P(R_\perp < R_{\rm true})$ as a function of $R_\perp$ for values of $R_{\rm true} = 50$ kpc (solid) and $R_{\rm true} = 100$ kpc (dashed), with different colors corresponding to different values of $\rho_{\rm DLA}$ as indicated in the legend. The points show the value of $P(R_\perp < R_{\rm true})$ corresponding to each sample sightline (although values of $P(R_\perp < R_{\rm true}) = 1$ are not plotted).

This figure demonstrates that for $\rho_{\rm DLA} \leqslant 20$ kpc, most sightlines having $R_\perp \leqslant 50$ kpc or $\leqslant 100$ kpc have a high probability of lying within $R_{\rm true} \leqslant 50$ kpc or $\leqslant 100$ kpc, respectively. For $\rho_{\rm DLA} = 20$ kpc, only 4 of 18 sightlines within $R_\perp < 100$ kpc have $P(R_\perp < 100$ kpc$) < 1$, and in three of these four cases $P(R_\perp < 100$ kpc$) \gtrsim 0.6$. Moreover, there are only two sightlines at $R_\perp > 100$ kpc with a non-zero $P(R_\perp < 100$ kpc), and these probability values are low ($\lesssim$0.35). Therefore, in coadded spectra of all CGM sightlines having $R_\perp \leqslant 100$ kpc, four of the sightlines will have a ~30%–50% probability of lying at $R_{\rm true} > 100$ kpc. Under the assumption that the CGM absorption strength declines with $R_{\rm true}$, the presumably weaker absorption in these few sightlines will tend to dilute the absorption signal measured in the coadded spectrum. At the same time, a coadded spectrum of sightlines with $R_\perp > 100$ kpc may include a few sightlines with $R_{\rm true} < 100$ kpc: specifically, two sightlines with $R_\perp > 100$ kpc have a ~25%–35% probability of having $R_{\rm true} < 100$ kpc. These sightlines therefore may tend to enhance the absorption signal measured at larger impact parameters.

These effects become more pronounced for larger values of $\rho_{\rm DLA}$. For instance, the average value of $P(R_\perp < 100$ kpc) for all sightlines with $R_\perp < 100$ kpc is 0.97 for $\rho_{\rm DLA} = 10$ kpc, 0.92 for $\rho_{\rm DLA} = 20$ kpc, 0.78 for $\rho_{\rm DLA} = 40$ kpc, and 0.61 for $\rho_{\rm DLA} = 70$ kpc. Similarly, the likelihood of spurious enhancement of the absorption signal at large $R_\perp$ increases with $\rho_{\rm DLA}$: the average value of $P(R_\perp < 100$ kpc) for all sightlines having $R_\perp > 100$ kpc is 0.04 for $\rho_{\rm DLA} = 20$ kpc and 0.12 for $\rho_{\rm DLA} = 70$ kpc.

In more qualitative terms, our uncertainty in the value of $R_{\rm true}$ for our sample sightlines can be considered an additional source of systematic uncertainty in our assessment of the average CGM absorption strength as a function of projected distance from the centers of DLA host halos. Under the assumption that this absorption declines in strength with $R_{\rm true}$, we expect that the primary repercussion of this uncertainty is a "dilution" or underestimation of the CGM absorption signal at small impact parameters. The foregoing analysis suggests that the enhancement of CGM absorption at large $R_\perp$ due to the inclusion of sightlines at small $R_{\rm true}$ occurs with a relatively low probability. Because $\rho_{\rm DLA}$ is not well constrained and may span a wide range of values, we do not attempt to correct for these effects here. However, they will be considered as we proceed with our comparison to previous results on the CGM

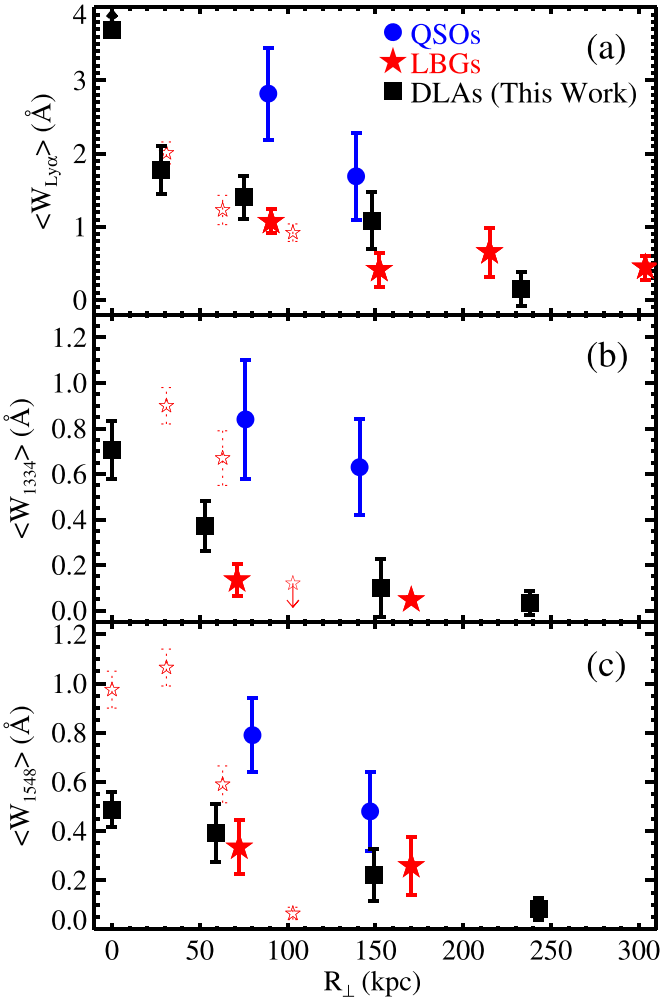

Figure 14. (a) $\langle W_{\rm Ly\alpha}\rangle$ measured in the coadded spectra generated as described in Section 3.2 of DLA (at $R_\perp = 0$ kpc) and CGM sightlines (black). Measurements of CGM absorption in coadded spectra of sightlines probing foreground QSO host halos are shown in blue (QPQ6; QPQ7). The CGM absorption strength around LBGs measured along background LBG sightlines is shown with open red stars (Steidel et al. 2010), and LBG-CGM absorption measured toward background QSOs is indicated with solid red stars (Adelberger et al. 2005; Simcoe et al. 2006; Rakic et al. 2011; Rudie et al. 2012; Crighton et al. 2014). The CGM around DLAs exhibits $\langle W_{\rm Ly\alpha}\rangle$ similar to the material surrounding LBGs. (b) Same as panel (a), for $\langle W_{1334}\rangle$. The CGM around DLAs generally yields $\langle W_{1334}\rangle$ consistent with the CGM absorption strength measured around LBGs, although the DLA-CGM $\langle W_{1334}\rangle$ at $R_\perp \sim 50$ kpc is marginally discrepant with both measurements of the LBG-CGM at $R_\perp \sim 60$–70 kpc shown. (c) Same as panel (a), for $\langle W_{1548}\rangle$.

absorption strength around optically selected samples. We also note that the cosmological hydrodynamical simulations of Rahmati & Schaye (2014) predict that the vast majority of DLAs are located with $\lesssim$10 kpc of the nearest galaxy, supportive of a scenario in which $\rho_{\rm DLA}$ has a small value in the context of the range of distances considered above.

5.2.2. Comparison with the CGM around Bright Galaxies and QSOs

Figure 14 shows $\langle W_{\rm Ly\alpha}\rangle$ (a), $\langle W_{1334}\rangle$ (b), and $\langle W_{1548}\rangle$ (c) measured from the coadded spectra in Figure 4 (black squares). Symbols at $R_\perp = 0$ kpc show equivalent widths measured in the coadded spectra of DLA sightlines. The absorption strength of CGM material around QSO host galaxies measured using a similar data set is shown with filled blue circles (QPQ6;

QPQ7). The CGM absorption strength around LBGs measured along coadded background galaxy sightlines is shown with red open stars (Steidel et al. 2010), and measurements of the LBG-CGM absorption strength toward background QSOs assembled from the literature (Adelberger et al. 2005; Simcoe et al. 2006; Rakic et al. 2011; Rudie et al. 2012; Crighton et al. 2014) are plotted with red filled stars.

First, regarding average equivalent widths measured along DLA sightlines, we find that they are significantly lower than equivalent widths measured down the barrel in coadded spectra of LBGs. In particular, Steidel et al. (2010) measure $\langle W_{1334}^{\rm LBG}\rangle = 1.6$–$1.8$ Å and $\langle W_{1526}^{\rm LBG}\rangle = 1.3$–$1.5$ Å, values more than twice as large as $\langle W_{1334}^{\rm DLA}\rangle$ and $\langle W_{1526}^{\rm DLA}\rangle$ (Figure 14; Table 3). The relatively low absorption strength in DLAs suggests that their low-ion absorption profiles are tracing material with less extreme kinematics on average. This may be a consequence of DLAs having lower host halo masses, particularly given the established correlation between $W_{1526}^{\rm DLA}$ and metallicity. However, Steidel et al. (2010) argued that the large LBG C II Si II equivalent widths are due to large-scale outflows driven by star formation in the galaxies based on the overall blueshift of the transitions (by $\sim 100-800$ km s^{-1}). The low $\langle W_{1334}^{\rm DLA}\rangle$ may therefore instead indicate either that DLA host galaxies drive less extreme outflows, or that these outflows are not traced by the low-ion absorption because, e.g., the DLAs are not co-spatial with galactic star formation (Fumagalli et al. 2014b).

Turning to the CGM, we find that the equivalent widths of CGM absorption around DLAs and LBGs are consistent within the measurement errors. With the exception of the $\langle W_{1334}^{\rm CGM}\rangle$ measurement at ∼50 kpc, which falls between the Steidel et al. (2010) value of $\langle W_{1334}\rangle$ at $R_\perp \sim 60$ kpc and the independent LBG-CGM measurement toward background QSOs at ∼70 kpc, every DLA-CGM $\langle W\rangle$ reported is within $\lesssim 1\sigma$ of the neighboring LBG-CGM value. This suggests that on average, both LBGs and DLAs are surrounded by similar gaseous environments, in spite of any differences in the distribution of halo masses and/or star formation histories among the two populations. We additionally note that the cosmological "zoom-in" simulations of Faucher-Giguère et al. (2014) predict this overall similarity, under the assumption that DLAs do indeed occupy smaller halos than bright LBGs. In particular, these authors report that the covering fraction of optically thick H I within $R_\perp < 100$ kpc remains approximately constant over a range in halo mass $M_{\rm h} \sim 10^{11-12}\,M_\odot$. They do not report $\langle W\rangle$ of Lyα or metal-line absorption in the simulated CGM; however, we expect comparisons with more detailed predictions from such work to yield useful constraints on the physics adopted by the simulations.

Furthermore, the significant decline in both $\langle W_{\rm Ly\alpha}\rangle$ and $W_{\rm Ly\alpha}$ with $R_\perp$ measured in our DLA-CGM sightlines is similar to the trend exhibited in nearly all studies of CGM absorption centered around magnitude-selected systems. This finding conflicts with a picture in which DLAs are dominated by absorption on the outskirts ($R_\perp \sim 100$ kpc) of the halos hosting bright LBGs, and instead suggests that DLAs tend to arise close to the centers of their halos. Moreover, as discussed in Section 5.2.1, if there is indeed a small offset between the DLA locations and their halo centers, the CGM absorption signal at a given $R_{\rm true}$ will likely be underestimated. This suggests that the consistency between DLA-CGM and LBG-CGM absorption measurements cannot be due to spurious sampling of regions with small $R_{\rm true}$, and is robust to the systematic scatter introduced by our experimental design.

In contrast to the LBG-CGM, the CGM around QSOs exhibits marginally stronger absorption in both low- and high-ionization transitions than that around DLAs. The QSO-CGM $\langle W_{\rm Ly\alpha}\rangle$ value at $R_\perp = 89$ kpc is 2.0σ higher than the measured DLA-CGM absorption at comparable projected distances. The QSO-CGM $\langle W_{1334}\rangle$ is likewise ~ 1.7–2.1σ stronger than our measurements of $\langle W_{1334}\rangle$ at $R_\perp \lesssim 200$ kpc from DLAs. The general finding that the CGM around QSOs gives rise to the strongest absorption in low-ionization transitions (i.e., Lyα, C II) of any galaxy environment probed to date was discussed in detail in QPQ7, and the absorption in DLA environments assessed here offers no exception. Indeed, it was noted in QPQ7 that QSO host halos exhibit the strongest low-ionization CGM both at a given $R_\perp$ and at a given $R_\perp/R_{\rm vir}$ (with an adopted fiducial QSO host halo virial radius $R_{\rm vir}^{\rm QSO} \sim 160$ kpc). Furthermore, it was argued that this strong, cool gas absorption must result primarily from the relatively high masses of the halos hosting QSOs (White et al. 2012). The QSO-CGM and DLA-CGM $\langle W_{1548}\rangle$ values lie in somewhat closer agreement, but are still discrepant by ~ 1.3–2.1σ within $R_\perp < 200$ kpc. This apparent enhancement is likely also driven by the high host halo masses of QSOs, and our finding that C IV-absorbing material is distributed over large scales (Section 4.4) and is therefore likely tracing virial halo motions lends further support to this explanation.

The comparisons described above offer new insight into the origin of metals extending many tens to hundreds of kiloparsecs from galaxies at $z \sim 2$. Metal absorption in LBG environments has been attributed in the literature to powerful, metal-rich gas outflows driven to >100 kpc distances by strong star formation activity in the central galaxy (Steidel et al. 2010). Bright LBGs, with typical SFRs $\sim 20-50\ M_\odot$ yr^{-1} (e.g., Erb et al. 2006b), do indeed exhibit strong outflows when observed down the barrel, with metal-line absorption extending blueward of systemic velocity by up to ∼800 km s^{-1} (Steidel et al. 2010). However, the spatial extent and ultimate fate of this high-velocity material has remained unconstrained: to give rise to the observed blue-shifted absorption, it need only cover the young stars in the LBGs extending over scales of a few kiloparsecs (Rubin et al. 2014).

Adding a new layer to this picture, the present study has revealed a strong similarily between the CGM metal absorption strength around both LBGs and DLAs; that is, in the environments surrounding galaxies with SFRs which differ by at least an order of magnitude. In particular, Fumagalli et al. (2015) placed a limit on the in situ SFR of typical DLAs within ∼6 kpc of the QSO sightlines of $\lesssim 0.65\ M_\odot$ yr^{-1}, and further determined that only a small minority of DLAs (<13%) have SFRs $>2\ M_\odot$ yr^{-1} within ∼10 kpc. We consider it implausible that systems with such low SFRs could give rise to powerful gas outflows similar to those attributed to bright LBGs, and yet the material in their surroundings exhibits very similar C II and C IV absorption strengths.

This suggests an alternative origin for the metals in *both* the LBG- and DLA-CGM. Of course, some fraction of the DLA population is certainly in the vicinity of LBGs, allowing the possibility that the DLA-CGM is on occasion enriched by LBG winds. The probability of such enrichment may be estimated by invoking the cross-correlation function between DLAs and

LBGs measured in Cooke et al. (2006) and the LBG luminosity function of Reddy et al. (2008). We find that a spherical volume extending 100 proper kpc from a DLA at $z = 2.5$ has only a ∼10% probability of containing a bright ($R < 25.5$) LBG. The vast majority of DLAs, therefore, appear to lie well beyond a plausible enrichment "radius" from ongoing, LBG-driven galactic outflows. Alternative enrichment mechanisms for LBG and DLA environments could include tidal stripping or the accretion of gas which has been enriched and expelled from dwarf galaxies at an earlier epoch (Shen et al. 2013). We discuss these scenarios in more detail along with additional supporting evidence in the next subsection. Finally we note that DLAs are known to be ubiquitously associated with strong O VI absorption at $2 < z < 4$ (Lehner et al. 2014). The velocity profiles of this highly ionized material are kinematically complex and tend to be broader than absorption in C IV. Lehner et al. (2014) concluded from this lack of coherence that the O VI absorption likely traces a distinct, collisionally ionized gas phase and suggested that such a phase may arise from the interaction between shock-heated outflows and a cooler ambient CGM. These findings are suggestive that DLAs are indeed capable of driving large-scale outflows in spite of their low SFR. However, they also bolster our conclusion that the C IV absorption associated with DLAs does not trace such putative winds.

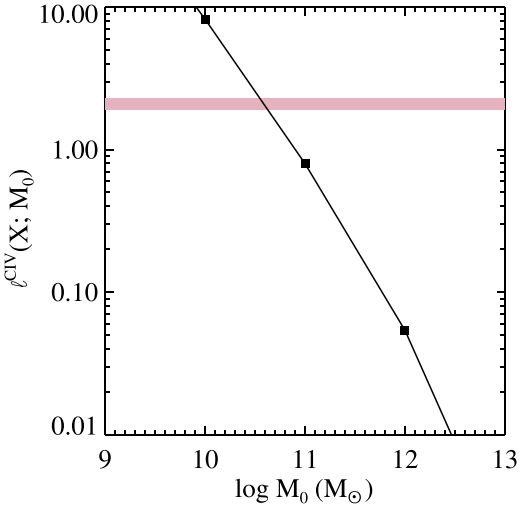

Figure 15. Predicted incidence of strong ($W_{1548} > 0.3$ Å) C IV assuming every dark matter halo with mass $>M_0$ hosts a DLA and is surrounded by $W_{1548} > 0.3$ Å absorption with a covering fraction $f_C = 50\%$ to $R_{C\,IV} = 100$ kpc. The pink band shows the observed random incidence of C IV having $W_{1548} > 0.3$ Å (QPQ7). If every DLA contributes to the random incidence of C IV absorption in this manner, the DLA population must predominantly arise in halos with masses $\gtrsim 10^{10.5}$ $M_\odot$.

5.3. The C IV Halos of DLAs

In Section 4.3, we emphasized the high covering fraction of strong C IV around DLAs: ≈57% for $R_\perp < 100$ kpc. We showed that the C IV equivalent widths along the CGM sightlines frequently exceed half that measured along the corresponding DLA sightline. These properties imply a ubiquitous, highly ionized, and enriched medium tracing the environments surrounding DLAs. Investigating further, in Section 4.4 we demonstrated a high degree of kinematic coherence between the C IV absorption along each pair of sightlines. This coherence is exemplified by the small offsets in the flux-weighted velocity centroids of these profiles, which are <60 km s^{-1} for 8 of 12 pairs and never exceed 105 km s^{-1} over projected distances as large as $R_\perp = 176$ kpc. Finally, inspired by the similarity between the LBG- and DLA-CGM absorption discussed in Section 5.2.2, we note that Turner et al. (2014) detected enhanced C IV absorption out to 2 Mpc from their LBG sample. While this absorption is weak (0.01 Å $< \langle W_{1548} \rangle <$ 0.1 Å at 200 kpc $< R_\perp < 2$ Mpc), this finding nevertheless suggests that the C IV absorption around DLAs may in fact extend to much larger scales than are probed in this study.

Together, these results offer unique constraints on the formation and evolution of C IV "halos." On the one hand, the high incidence of C IV requires wide-spread enrichment in the highly ionized gas phase. Previous works have invoked strong galactic winds to enrich halo gas and drive the material to large scales (e.g., Aguirre et al. 2001; Oppenheimer & Davé 2006). Some have further argued that the C IV observed along sightlines probing DLAs directly traces the wind (Fox et al. 2007a). However, such a scenario lies in apparent conflict with the kinematics of the C IV-absorbing gas associated with DLAs. First, the coherence in kinematics between sightlines of a given pair implies modest motions within the C IV-absorbing medium. Wind speeds exceeding 100 km s^{-1} are likely ruled out by the observations, unless one invokes a fine-tuned geometry to minimize velocity differences at ∼100 kpc separations. Second, the C IV absorption appears to be dominated by gas extending over large distances. The large covering fraction of $W_{1548}^{CGM} > 0.2$ Å absorption evident in Figure 8, along with the ∼60% frequency with which $\eta_{1548} > 0.5$ (Figure 9(c)), imply that the properties are largely determined by gas at $R_{3D} \sim 30$–100 kpc. Such a geometry in turn implies a limited contribution from galactic wind kinematics, which we expect to dominate on smaller scales (i.e., close to the star-forming regions). Considering these points together, we regard a wind-dominated scenario as implausible and encourage comparison of these observations to models of galaxy formation that invoke high mass-loading factors in feedback from lower mass galaxies (e.g., Vogelsberger et al. 2013, 2014, Crain et al. 2015.

In lieu of winds, what may the C IV gas be tracing? Reviewing the properties, one requires a medium that was previously enriched, that is distributed over scales of ∼100 kpc, and has relatively quiescient kinematics. Perhaps the simplest picture to invoke is a highly ionized medium that pervades the dark matter halos hosting DLAs and in many cases extends beyond the virial radii of these halos. One may envision a filamentary structure of diffuse, enriched gas that expresses C IV and has kinematics dominated by gravitational motions, similar to the scenario first proposed by Rauch et al. (1997). Indeed, recent cosmological zoom simulations focusing on the formation of dwarf galaxies find that the mass loading of their outflows is significantly higher than the mass-loading of winds from LBG-like systems, enabling them to efficiently enrich the IGM (Shen et al. 2014). The early enrichment of filamentary infalling material may also explain the high metallicities of weak (0.3 Å $< W_{2796} < 1$ Å) Mg II absorbers at high redshifts ($z > 2$; Matejek et al. 2013). Rauch et al. (1997) additionally showed that such structures can naturally give rise to a broad range in C IV velocity widths, depending on their geometry and the orientation of the line of sight. We do note at least one potential conflict with this simple scenario. Observations along

DLA sightlines have shown that the kinematics of the C IV gas are more complex than those traced by the low-ionization gas. In the cases of DLAs exhibiting both very broad low- and high-ionization absorption, one may need to invoke additional motions on small scales (e.g., winds) to account for the measurements. The potential impact of winds on the DLA C IV absorption in such cases could in principle be tested by comparing the coherence of the C IV between paired sightlines with the same measurement in less extreme systems.

Irrespective of the origin of the C IV gas surrounding DLAs, we may leverage the high covering fraction to provide a constraint on the minimum mass of halos hosting DLAs as follows. We adopt two assumptions motivated by our observations and current theories on neutral gas in high-z galaxies: (1) we assume that all halos above a minimum mass M_0 contain sufficient H I gas to satisfy our DLA criterion ($N_{\rm H\,I} \geqslant 10^{20.1}\,{\rm cm}^{-2}$) and (2) we assume every halo hosting DLAs exhibits extended, strong C IV absorption with covering fraction $f_{\rm C}$ as observed in this study. Under these assumptions, we may calculate the incidence of strong C IV absorption as a function of M_0:

$$\ell^{\rm C\,IV}(X; M_0) = n_{\rm tot}(M_0) f_{\rm C}\, \pi R_{\rm C\,IV}^2, \quad (4)$$

where $R_{\rm C\,IV}$ is the extent of the C IV gas, $f_{\rm C}$ is the covering fraction for $R_\perp < R_{\rm C\,IV}$, and where $n_{\rm tot}(M_0)$ is the comoving number density of halos with $M_{\rm h} > M_0$.

Figure 15 presents $\ell^{\rm C\,IV}(X; M_0)$ assuming a ΛCDM cosmology at $z = 2.2$ with $f_{\rm C} = 0.5$ and $R_{\rm C\,IV} = 100$ kpc. The pink band overplotted on the figure shows the incidence of strong ($W_{1548} > 0.3$ Å) C IV systems at $z = 2.1$ along random quasar sightlines (QPQ7). We find that $\ell^{\rm C\,IV}(X; M_0)$ exceeds the random value for $M_0 < 10^{10.5}\ M_\odot$. This constraint is conservative in the sense that strong C IV absorption may also occur in astrophysical sightlines located far from DLAs. However, our assumption that DLAs occupy all halos with masses $>M_0$ may not hold in practice, and relaxing this assumption would indeed allow for a contribution to the DLA population from halos with $M_{\rm h} < M_0$.

The high incidence of strong C IV absorption and the large scales over which it is distributed point to a substantial reservoir of metals in the diffuse material surrounding DLAs at $z \sim 2$. We may roughly estimate the total mass in carbon in this CGM reservoir as follows:

$$M_{\rm C}^{\rm CGM} = \pi f_{\rm C} R_{\rm C\,IV}^2 \langle N_{\rm C\,IV} \rangle m_{\rm C} \frac{1}{x_{\rm C\,IV}},$$

where $x_{\rm C\,IV} = N_{\rm C\,IV}/N_{\rm C}$ and $m_{\rm C}$ is the mass of the carbon atom. Here we conservatively set $x_{\rm C\,IV} = 0.3$, as Fox et al. (2007b) demonstrated this to be the maximum possible ionization fraction in models assuming either photo- or collisional ionization. Adopting a typical column density of $\langle N_{\rm C\,IV} \rangle = 10^{14}\,{\rm cm}^{-2}$ for C IV in DLAs (Fox et al. 2007a), with $f_{\rm C} = 0.5$ and $R_{\rm C\,IV} = 100$ kpc as above, we find $M_{\rm C}^{\rm CGM} \approx 5 \times 10^5\ M_\odot$.

We compare this value to an estimate of the total mass in carbon in the stars and neutral ISM of DLAs themselves. We first assume that DLAs occupy dark matter halos having masses $M_{\rm h} = 10^{11.5}\ M_\odot$ (only slightly lower in mass than the halos hosting LBGs, e.g., Rakic et al. 2013). Such halos host galaxies having stellar masses $M_*^{\rm DLA} \approx 10^{9.3}\ M_\odot$ at $z \sim 2$ (Moster et al. 2013), and which are likely to have high ISM gas fractions $f_{\rm gas} \gtrsim 0.5$ (Tacconi et al. 2013). The total baryonic mass of these systems is then $M_{\rm bar}^{\rm DLA} = \frac{1}{1 - f_{\rm gas}} M_*^{\rm DLA}$, and the total mass in carbon is

$$M_{\rm C}^{\rm DLA} = \frac{Z_{\rm DLA}}{Z_\odot} ({\rm C/H})_\odot \frac{1}{1 - f_{\rm gas}} M_*^{\rm DLA}.$$

If we assume a typical DLA metallicity of $\log \frac{Z_{\rm DLA}}{Z_\odot} = -1.5$ (Neeleman et al. 2013) and adopt a value for the solar abundance of carbon $({\rm C/H})_\odot = 10^{-3.57}$ (Asplund et al. 2009), we find $M_{\rm C}^{\rm DLA} \approx 3 \times 10^4\ M_\odot$, an order of magnitude lower than $M_{\rm C}^{\rm CGM}$. DLAs in less massive halos will likely have yet lower metallicities, and hence may be deficient in carbon relative to the solar abundance pattern (Cooke et al. 2011). We expect that the discrepancy between the carbon mass in the stars and ISM of such systems and the mass of carbon in their CGM will therefore be even more extreme.

The preceding estimates are crude, and suffer from uncertainties comparable to the differential between the two values obtained. However, the exercise illustrates that diffuse CGM material must make up an important fraction of the universal metal budget as early as 10 Gyr ago, and may contain more metals than the stellar material and star-forming regions it surrounds. Analysis of absorption from a yet more highly ionized CGM component traced by O VI is similarly suggestive that this CGM dominates the metal budget, and may contain as much as four times the mass in metals of DLAs as early as $z \sim 2.5$ (Lehner et al. 2014). This widespread distribution of metals, in combination with the apparent quiescence of the C IV kinematics, point to efficient enrichment processes occurring at much earlier times; e.g., powerful stellar feedback with high mass-loading factors from galaxies at $z \gtrsim 3$. We await deep, rest-frame UV spectroscopy of star-forming systems at $z > 3$, aided by gravitational lensing (e.g., Bayliss et al. 2013) or with next-generation 30 m class telescopes, to confirm this picture.

6. CONCLUSIONS

With the goal of understanding the relationship between reservoirs of neutral hydrogen and star formation at early times, we have searched spectroscopy of paired QSO sightlines with projected separations $R_\perp < 300$ kpc for instances of DLA absorption in the foreground. We use the second QSO sightline in each pair to characterize the Lyα and metal-line absorption as a function of $R_\perp$ around 40 such systems. Our primary findings are as follows:

1. Damped absorption rarely extends over scales $\gtrsim$10 kpc: the measured incidence of paired sightlines both exhibiting DLAs within $R_\perp < 100$ kpc is $f_{\rm C}^{\rm DLA} \sim 0.13$. This incidence, although low, is consistent with a model in which the cross section of DLAs increases with halo mass and extends over 1400 kpc^2 in halos with $M_{\rm h} = 10^{12}\ M_\odot$ (Font-Ribera et al. 2012).
2. We place a lower limit on the incidence of optically thick H I absorption within 200 kpc of DLAs of $\gtrsim$20%–40%. However, strong absorption from the low-ionization metal transition Si II 1526 is rare in these environments. Systems having $W_{1526}^{\rm CGM} > 0.2$ Å occur with an incidence

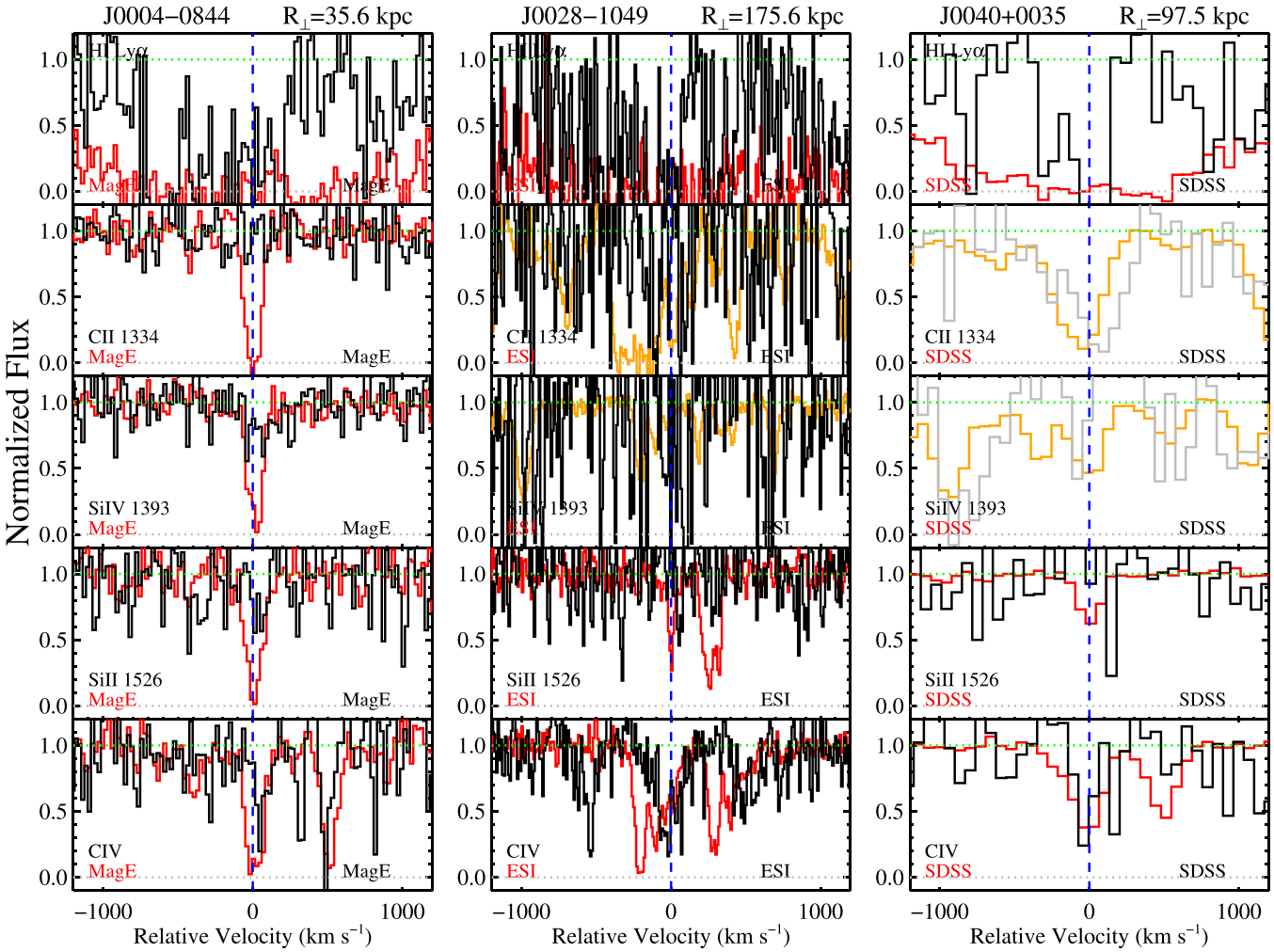

Figure 16. QSO pair spectroscopy for the 40 systems in our sample. Each column shows the Lyα, C II, Si IV, Si II, and C IV absorption transitions due to a DLA (red histogram). The black histogram shows the CGM absorption probed by the secondary QSO at the same redshift as the DLA. The blue vertical dashed lines show the rest velocities of the corresponding transitions. The physical separation of each pair and the QSO pair ID are given at the top of each column, and the instruments used to obtain the spectra shown in each panel are marked in red and black, respectively. Spectral regions covering metal transitions and falling in the Lyα forest are shown with orange (for DLAs) or gray (for CGM sightlines) histograms. Metal-line transitions affected by blending with unassociated systems are shown with dotted lines. A subset of our sample was observed at high spectral resolution (FWHM $\lesssim$50 km s^{-1}) with, e.g., Magellan/MagE or Keck/ESI. The majority of our pairs, however, were observed with medium-resolution setups (FWHM ~125–180 km s^{-1}; with Keck/LRIS, Gemini/GMOS, etc.).

of 20^{+12}_{-8}% within $R_\perp < 100$ kpc. These measurements suggest that the Si II absorption observed toward DLAs themselves primarily traces material within $R_\perp \lesssim 30$ kpc, rather than an extended gaseous halo.

3. We measure a high incidence (57^{+12}_{-13}%) of strong C IV absorption ($W_{1548}^{\rm CGM} > 0.2$ Å) within 100 kpc of DLAs, with the absorption strength in the CGM frequently at least half that in the nearby DLA. This absorption exhibits a high degree of kinematic coherence on scales of ~26–176 kpc, with the flux-weighted velocity centroids for each sightline pair offset by no more than <105 km s^{-1}. These profiles must arise predominantly from the motions of material at large physical separations from the DLAs; i.e., at $R_{\rm 3D}\sim$ 30–100 kpc. Under the assumption that all dark matter halos with masses above M_0 host DLAs, the ubiquity of C IV absorption in DLA environments requires that $M_0 \gtrsim 10^{10.5}\ M_\odot$.
4. The equivalent width of Lyα absorption in the DLA-CGM is anticorrelated with $R_\perp$ at >98% confidence. This finding suggests that most DLAs do not arise near the outskirts of bright LBG host halos, and instead are likely located close to their halo centers.
5. The average Lyα and metal absorption strength in the environments extending to 300 kpc from DLAs is of similar strength to that exhibited by the CGM around LBGs. This implies either (1) that the DLA population is dominated by systems hosted by halos similar in mass to those hosting LBGs ($M_{\rm h} \sim 10^{11.6-12}\ M_\odot$), or (2) CGM absorption strength at $z \sim 2$ does not change with halo mass over the range $10^{10.5}\ M_\odot \lesssim M_{\rm h} \lesssim 10^{12}\ M_\odot$.
6. The close conformity between the DLA- and LBG-CGM, in combination with recently reported limits on the SFRs of DLA hosts (Fumagalli et al. 2015), suggest that the distribution of metals in the outer regions of DLA- and LBG-host halos occurs via the dynamical accretion of previously enriched material rather than via ongoing cool gas outflows.

The foregoing discussion reports our initial efforts to constrain the properties of the diffuse DLA-CGM and to understand the physical processes relevant to its origin. Future

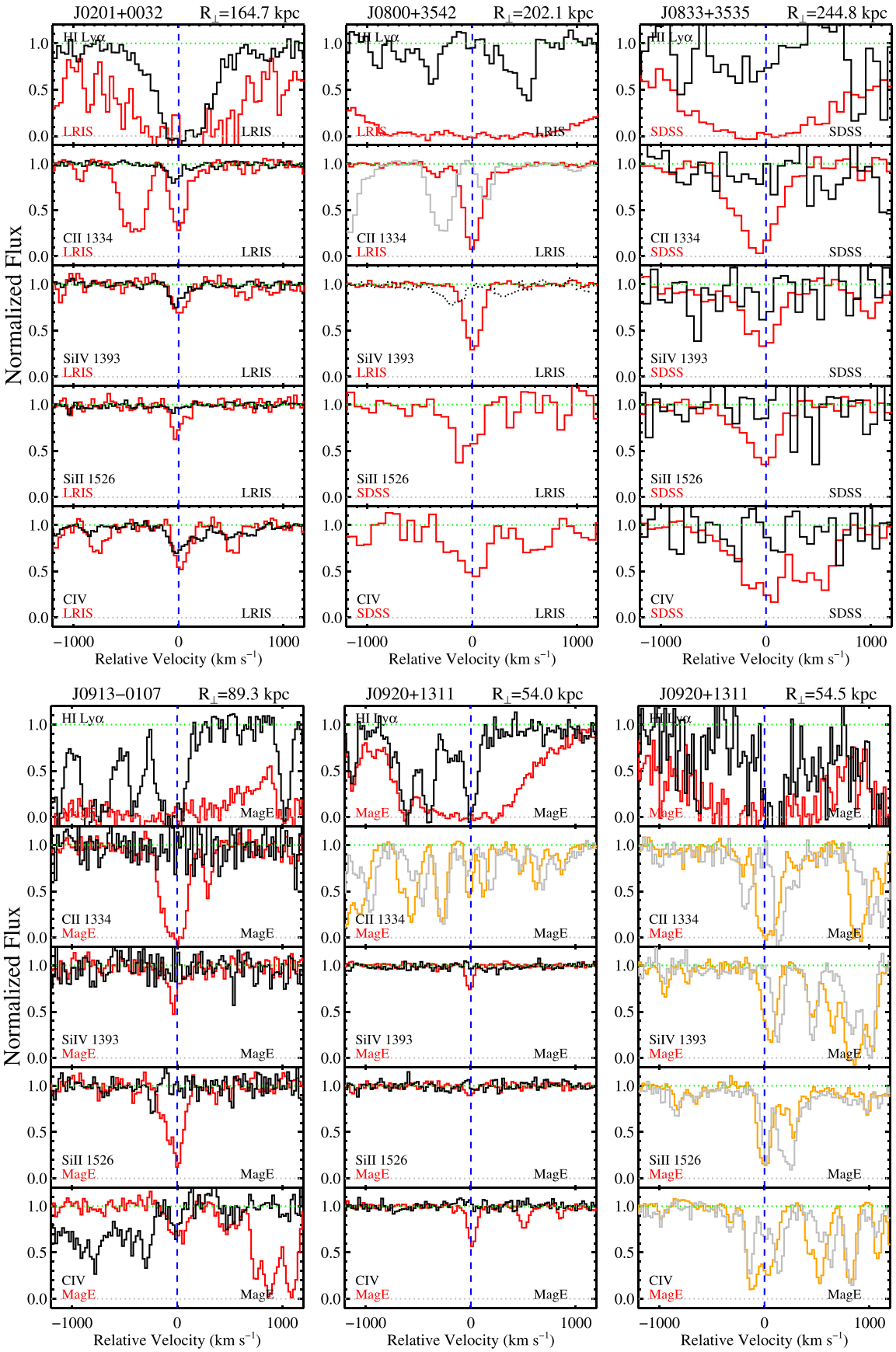

Figure 16. (Continued.)

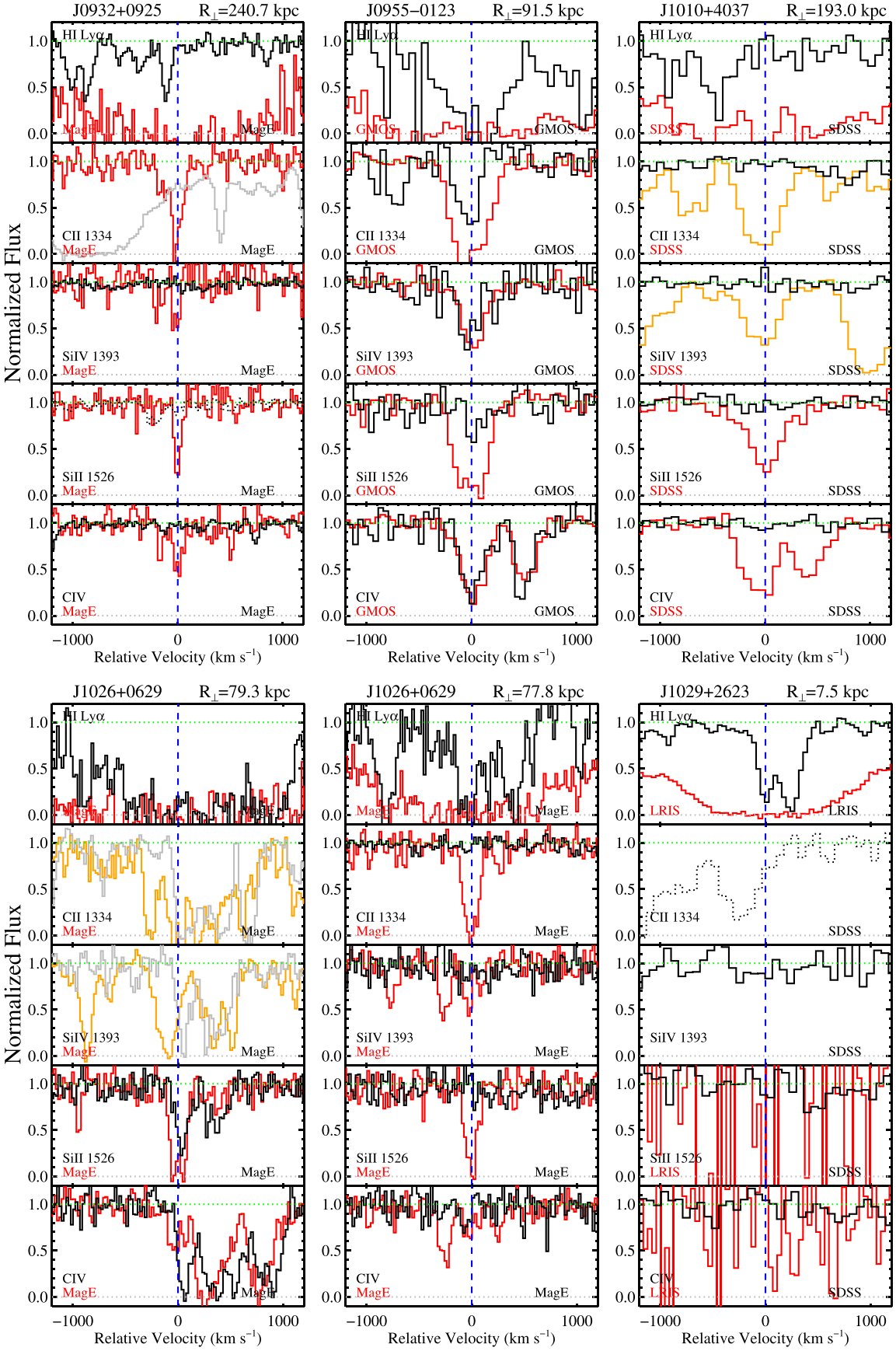

Figure 16. (Continued.)

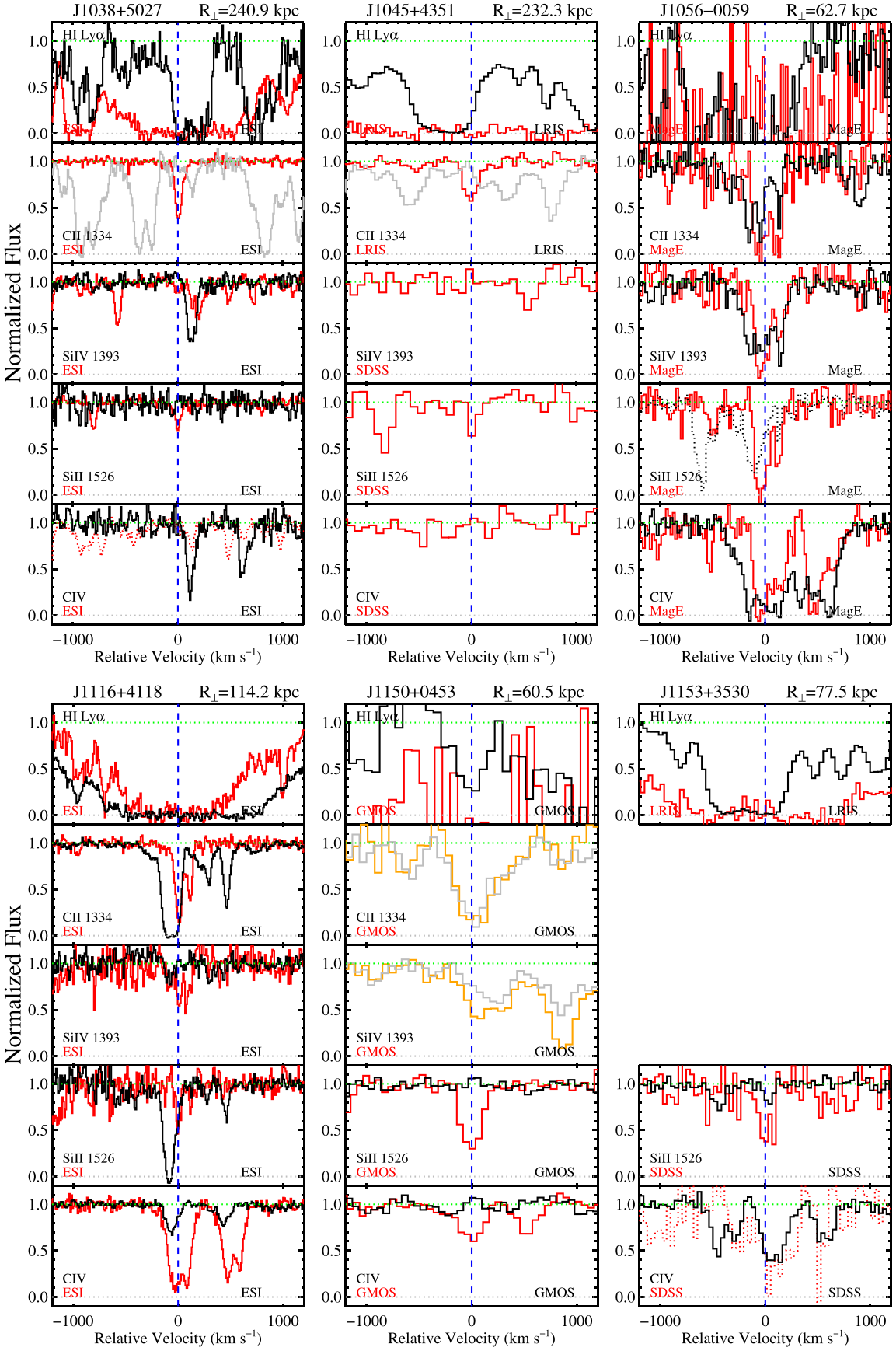

Figure 16. (Continued.)

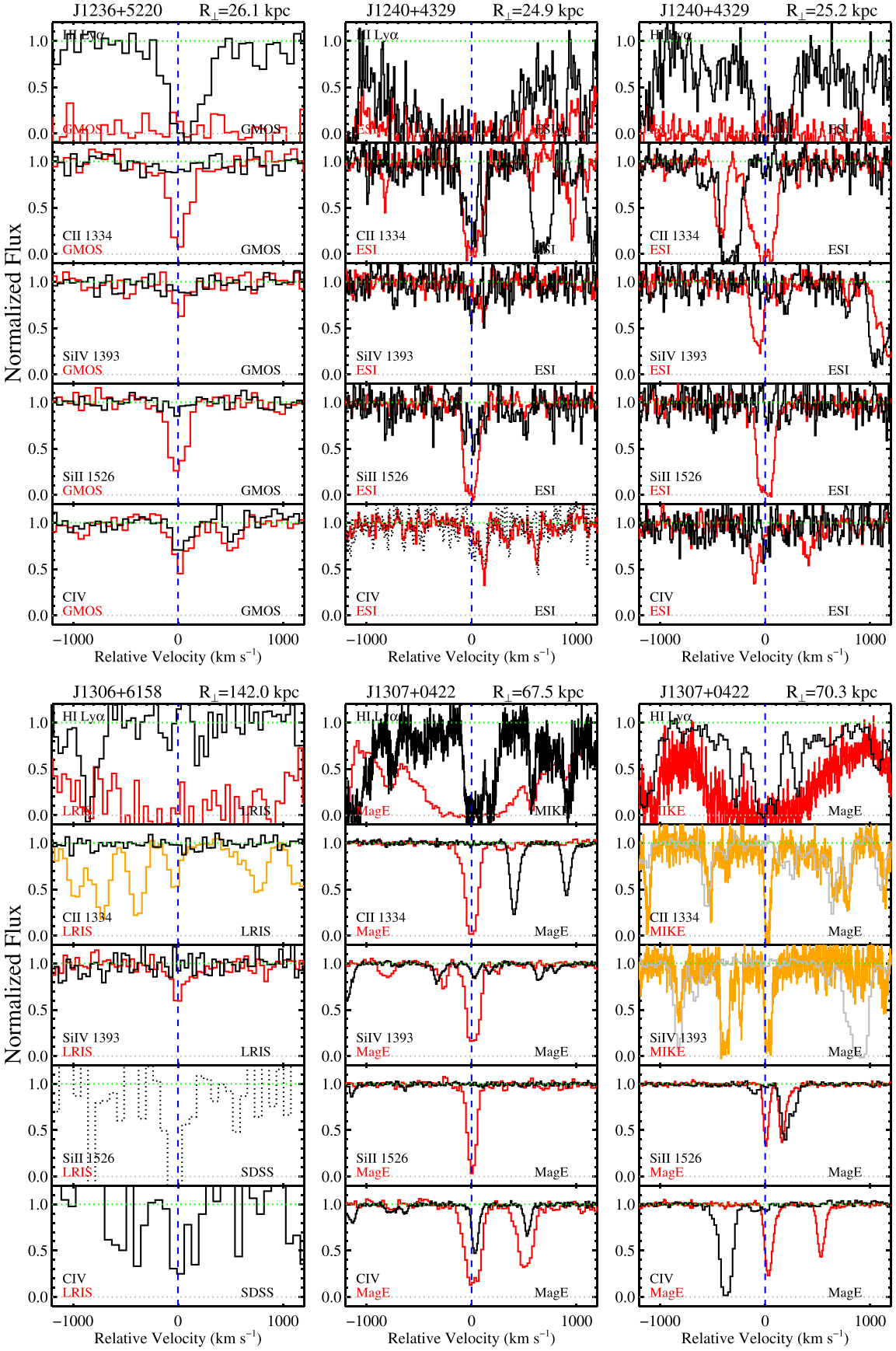

Figure 16. (Continued.)

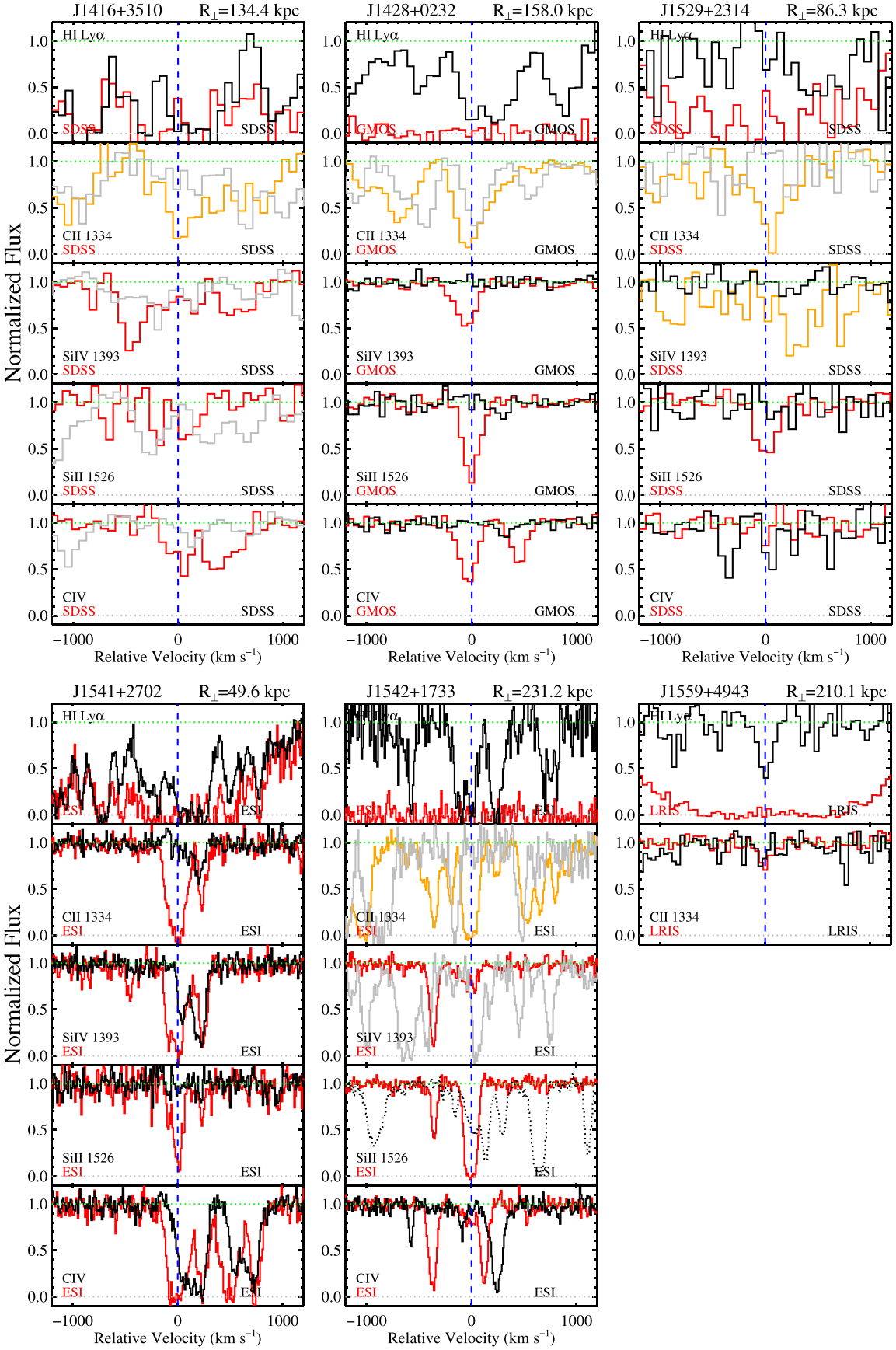

Figure 16. (Continued.)

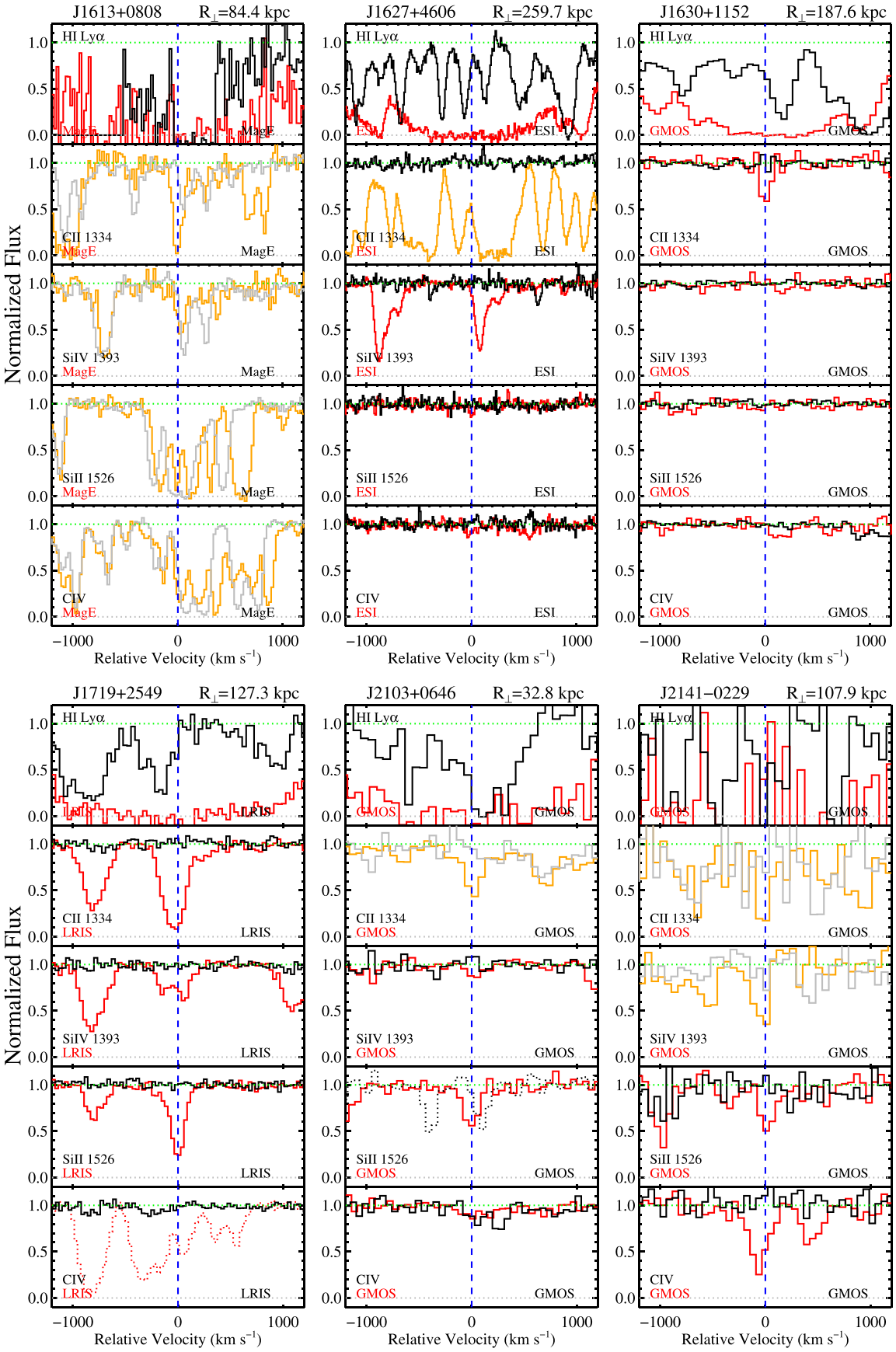

Figure 16. (Continued.)

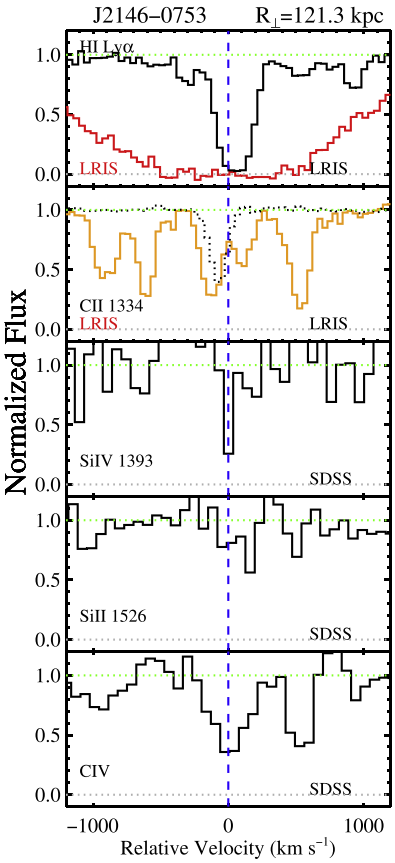

Figure 16. (Continued.)

directions will include analysis of detailed metal abundances and kinematics in our echellette-quality spectroscopy for constraints on the degree of CGM metal enrichment relative to that of DLA material. Direct comparisons of these results with the metal abundances and kinematics of CGM material around DLAs in cosmological zoom-in simulations (e.g., Shen et al. 2013; Faucher-Giguère et al. 2014) and simulations of large cosmological volumes (e.g., Bird et al. 2014; Vogelsberger et al. 2014) will inform future interpretation and provide crucial leverage on feedback prescriptions. In combination with ongoing efforts to characterize the emission from DLA hosts to deeper limits than have yet been achieved (e.g., Fumagalli et al. 2015), these experiments will ultimately link the early reservoirs of neutral material with the formation of luminous structures on every mass scale.

The authors wish to thank Sara Ellison, Crystal Martin, and George Djorgovski for aiding in collection and reduction of the Keck/ESI spectroscopy used in this study. We also wish to thank the anonymous referee for useful comments which improved the manuscript. It is our pleasure to thank Neil Crighton, Simeon Bird, Jeff Cooke, Claude-André Faucher-Giguère, Michele Fumagalli, John O'Meara, Celine Péroux, Ali Rahmati, and Sijing Shen for valuable discussion of this work, and to acknowledge Sijing Shen for sharing the results of her analysis of the CGM properties of the Eris2 simulation. Finally, we are grateful to Art Wolfe for sharing his insight on these results and for his inspiring and pioneering work in this field. K.H.R.R. acknowledges the generous support of the Clay Postdoctoral Fellowship, and J.F.H. acknowledges support from the Alexander von Humboldt foundation in the context of the Sofja Kovalevskaja Award. The Humboldt foundation is funded by the German Federal Ministry for Education and Research. J.X.P. and M.L. acknowledge support from National Science Foundation (NSF) grants AST-1010004, AST-1109452, AST-1109447, and AST-1412981. This paper includes data gathered with the 6.5 m Magellan Telescopes located at Las Campanas Observatory, Chile. Some of the data presented herein were obtained at the W.M. Keck Observatory, which is operated as a scientific partnership among the California Institute of Technology, the University of California, and the National Aeronautics and Space Administration. The Observatory was made possible by the generous financial support of the W.M. Keck Foundation. The authors wish to recognize and acknowledge the very significant cultural role and reverence that the summit of Mauna Kea has always had within the indigenous Hawaiian community. We are most fortunate to have the opportunity to conduct observations from this mountain.

APPENDIX

Figure 16 shows our spectroscopy of all DLAs and the corresponding CGM systems included in this study.

REFERENCES

Abazajian, K. N., Adelman-McCarthy, J. K., Agüeros, M. A., et al. 2009, ApJS, 182, 543
Adelberger, K. L., Shapley, A. E., Steidel, C. C., et al. 2005, ApJ, 629, 636
Adelberger, K. L., Steidel, C. C., Shapley, A. E., et al. 2004, ApJ, 607, 226
Aguirre, A., Hernquist, L., Schaye, J., et al. 2001, ApJ, 560, 599
Ahn, C. P., Alexandroff, R., Allende Prieto, C., et al. 2012, ApJS, 203, 21
Asplund, M., Grevesse, N., Sauval, A. J., & Scott, P. 2009, ARA&A, 47, 481
Bayliss, M. B., Rigby, J. R., Sharon, K., et al. 2014, ApJ, 790, 144
Bird, S., Haehnelt, M., Neeleman, M., et al. 2015, MNRAS, 447, 1834
Bird, S., Vogelsberger, M., Haehnelt, M., et al. 2014, MNRAS, 445, 2313
Bordoloi, R., Tumlinson, J., Werk, J. K., et al. 2014, ApJ, 796, 136
Bouché, N., Murphy, M. T., Péroux, C., et al. 2012, MNRAS, 419, 2
Bovy, J., Hennawi, J. F., Hogg, D. W., et al. 2011, ApJ, 729, 141
Bovy, J., Myers, A. D., Hennawi, J. F., et al. 2012, ApJ, 749, 41
Cen, R. 2012, ApJ, 748, 121
Chen, H.-W., Helsby, J. E., Gauthier, J.-R., et al. 2010, ApJ, 714, 1521
Churchill, C. W., Trujillo-Gomez, S., Nielsen, N. M., & Kacprzak, G. G. 2013, ApJ, 779, 87
Conroy, C., Shapley, A. E., Tinker, J. L., Santos, M. R., & Lemson, G. 2008, ApJ, 679, 1192
Cooke, J., Wolfe, A. M., Gawiser, E., & Prochaska, J. X. 2006, ApJ, 652, 994
Cooke, R., Pettini, M., Steidel, C. C., King, L. J., Rudie, G. C., & Rakic, O. 2010, MNRAS, 409, 679
Cooke, R., Pettini, M., Steidel, C. C., Rudie, G. C., & Nissen, P. E. 2011, MNRAS, 417, 1534
Crain, R. A., Schaye, J., Bower, R. G., et al. 2015, MNRAS, 450, 1937
Crighton, N. H. M., Hennawi, J. F., & Prochaska, J. X. 2013, ApJL, 776, L18
Crighton, N. H. M., Hennawi, J. F., Simcoe, R. A., et al. 2015, MNRAS, 446, 18
Ellison, S. L., Hennawi, J. F., Martin, C. L., & Sommer-Larsen, J. 2007, MNRAS, 378, 801
Erb, D. K., Shapley, A. E., Pettini, M., et al. 2006, ApJ, 644, 813
Erb, D. K., Steidel, C. C., Shapley, A. E., et al. 2006, ApJ, 647, 128
Faucher-Giguère, C.-A., Hopkins, P. F., Kereš, D., et al. 2015, MNRAS, 449, 987
Font-Ribera, A., Arnau, E., Miralda-Escudé, J., et al. 2013, JCAP, 5, 18
Font-Ribera, A., Miralda-Escudé, J., Arnau, E., et al. 2012, JCAP, 11, 59
Fox, A. J., Ledoux, C., Petitjean, P., & Srianand, R. 2007, A&A, 473, 791
Fox, A. J., Petitjean, P., Ledoux, C., & Srianand, R. 2007, A&A, 465, 171
Fumagalli, M., Hennawi, J. F., Prochaska, J. X., et al. 2014, ApJ, 780, 74
Fumagalli, M., O'Meara, J. M., Prochaska, J. X., Kanekar, N., & Wolfe, A. M. 2014b, MNRAS, 444, 1282

Fumagalli, M., O'Meara, J. M., Prochaska, J. X., Rafelski, M., & Kanekar, N. 2015, MNRAS, 446, 3178
Fumagalli, M., O'Meara, J. M., Prochaska, J. X., & Worseck, G. 2013, ApJ, 775, 78
Fumagalli, M., Prochaska, J. X., Kasen, D., et al. 2011, MNRAS, 418, 1796
Fynbo, J. P. U., Geier, S. J., Christensen, L., et al. 2013, MNRAS, 436, 361
Fynbo, J. P. U., Laursen, P., Ledoux, C., et al. 2010, MNRAS, 408, 2128
Haehnelt, M. G., Steinmetz, M., & Rauch, M. 1998, ApJ, 495, 647
Heckman, T. M., Armus, L., & Miley, G. K. 1990, ApJS, 74, 833
Hennawi, J. F., Myers, A. D., Shen, Y., et al. 2010, ApJ, 719, 1672
Hennawi, J. F., & Prochaska, J. X. 2007, ApJ, 655, 735
Hennawi, J. F., & Prochaska, J. X. 2013, ApJ, 766, 58
Hennawi, J. F., Prochaska, J. X., Burles, S., et al. 2006b, ApJ, 651, 61
Hennawi, J. F., Strauss, M. A., Oguri, M., et al. 2006a, ApJ, 651, 61
Hopkins, A. M., & Beacom, J. F. 2006, ApJ, 651, 142
Inada, N., Oguri, M., Morokuma, T., et al. 2006, ApJL, 653, L97
Jorgenson, R. A., & Wolfe, A. M. 2014, ApJ, 785, 16
Krogager, J.-K., Fynbo, J. P. U., Møller, P., et al. 2012, MNRAS, 424, L1
Lehner, N., O'Meara, J. M., Fox, A. J., et al. 2014, ApJ, 788, 119
Lopez, S., Reimers, D., Gregg, M. D., et al. 2005, ApJ, 626, 767
Maller, A. H., Prochaska, J. X., Somerville, R. S., & Primack, J. R. 2001, MNRAS, 326, 1475
Marshall, J. L., Burles, S., Thompson, I. B., et al. 2008, Proc. SPIE, 7014, 701454
Martin, C. L., Scannapieco, E., Ellison, S. L., et al. 2010, ApJ, 721, 174
Matejek, M. S., Simcoe, R. A., Cooksey, K. L., & Seyffert, E. N. 2013, ApJ, 764, 9
Möller, P., Fynbo, J. P. U., & Fall, S. M. 2004, A&A, 422, L33
Møller, P., Fynbo, J. P. U., Ledoux, C., & Nilsson, K. K. 2013, MNRAS, 430, 2680
Monier, E. M., Turnshek, D. A., & Rao, S. 2009, MNRAS, 397, 943
Moster, B. P., Naab, T., & White, S. D. M. 2013, MNRAS, 428, 3121
Nagamine, K., Springel, V., & Hernquist, L. 2004, MNRAS, 348, 421
Neeleman, M., Wolfe, A. M., Prochaska, J. X., & Rafelski, M. 2013, ApJ, 769, 54
Noterdaeme, P., Laursen, P., Petitjean, P., et al. 2012, A&A, 540, A63
Noterdaeme, P., Petitjean, P., Pâris, I., et al. 2014, A&A, 566, A24
Oguri, M., Schrabback, T., Jullo, E., et al. 2013, MNRAS, 429, 482
Oppenheimer, B. D., & Davé, R. 2006, MNRAS, 373, 1265
Péroux, C., Bouché, N., Kulkarni, V. P., York, D. G., & Vladilo, G. 2011, MNRAS, 410, 2237
Pettini, M., Rix, S. A., Steidel, C. C., et al. 2002, ApJ, 569, 742
Pontzen, A., Governato, F., Pettini, M., et al. 2008, MNRAS, 390, 1349
Prochaska, J. X., Chen, H.-W., Wolfe, A. M., Dessauges-Zavadsky, M., & Bloom, J. S. 2008, ApJ, 672, 59
Prochaska, J. X., Gawiser, E., Wolfe, A. M., Cooke, J., & Gelino, D. 2003, ApJS, 147, 227
Prochaska, J. X., Hennawi, J. F., Lee, K.-G., et al. 2013, ApJ, 776, 136
Prochaska, J. X., Hennawi, J. F., & Simcoe, R. A. 2013, ApJL, 762, L19
Prochaska, J. X., Wingyee Lau, M., & Hennawi, J. F. 2014, ApJ, 796, 146
Prochaska, J. X., & Wolfe, A. M. 1996, ApJ, 470, 403
Prochaska, J. X., & Wolfe, A. M. 1997, ApJ, 487, 73
Rahmati, A., & Schaye, J. 2014, MNRAS, 438, 529
Rakic, O., Schaye, J., Steidel, C. C., & Rudie, G. C. 2011, MNRAS, 414, 3265
Rakic, O., Schaye, J., Steidel, C. C., et al. 2013, MNRAS, 433, 3103
Rauch, M., Haehnelt, M. G., & Steinmetz, M. 1997, ApJ, 481, 601
Rauch, M., Sargent, W. L. W., & Barlow, T. A. 2001, ApJ, 554, 823
Razoumov, A. O., Norman, M. L., Prochaska, J. X., et al. 2008, ApJ, 683, 149
Razoumov, A. O., & Sommer-Larsen, J. 2006, ApJL, 651, L89
Reddy, N. A., Steidel, C. C., Pettini, M., et al. 2008, ApJS, 175, 48
Rubin, K. H. R., Prochaska, J. X., Koo, D. C., et al. 2014, ApJ, 794, 156
Rudie, G. C., Steidel, C. C., Trainor, R. F., et al. 2012, ApJ, 750, 67
Shapley, A. E., Steidel, C. C., Pettini, M., & Adelberger, K. L. 2003, ApJ, 588, 65
Sheinis, A. I., Bolte, M., Epps, H. W., et al. 2002, PASP, 114, 851
Shen, S., Madau, P., Conroy, C., Governato, F., & Mayer, L. 2014, ApJ, 792, 99
Shen, S., Madau, P., Guedes, J., Mayer, L., & Prochaska, J. X. 2013, ApJ, 765, 89
Simcoe, R. A., Sargent, W. L. W., Rauch, M., & Becker, G. 2006, ApJ, 637, 648
Smette, A., Robertson, J. G., Shaver, P. A., et al. 1995, A&AS, 113, 199
Steidel, C. C., Adelberger, K. L., Shapley, A. E., et al. 2003, ApJ, 592, 728
Steidel, C. C., Erb, D. K., Shapley, A. E., et al. 2010, ApJ, 717, 289
Steidel, C. C., Shapley, A. E., Pettini, M., et al. 2004, ApJ, 604, 534
Storrie-Lombardi, L. J., & Wolfe, A. M. 2000, ApJ, 543, 552
Tacconi, L. J., Neri, R., Genzel, R., et al. 2013, ApJ, 768, 74
Tremonti, C. A., Heckman, T. M., Kauffmann, G., et al. 2004, ApJ, 613, 898
Turner, M. L., Schaye, J., Steidel, C. C., Rudie, G. C., & Strom, A. L. 2014, MNRAS, 445, 794
Veilleux, S., Cecil, G., & Bland-Hawthorn, J. 2005, ARA&A, 43, 769
Veilleux, S., Shopbell, P. L., Rupke, D. S., Bland-Hawthorn, J., & Cecil, G. 2003, AJ, 126, 2185
Vogelsberger, M., Genel, S., Sijacki, D., et al. 2013, MNRAS, 436, 3031
Vogelsberger, M., Genel, S., Springel, V., et al. 2014, MNRAS, 444, 1518
Weiner, B. J., Willmer, C. N. A., Faber, S. M., et al. 2006, ApJ, 653, 1027
Werk, J. K., Prochaska, J. X., Tumlinson, J., et al. 2014, ApJ, 792, 8
White, M., Myers, A. D., Ross, N. P., et al. 2012, MNRAS, 424, 933
Wild, V., Kauffmann, G., White, S., et al. 2008, MNRAS, 388, 227
Wolfe, A. M., Gawiser, E., & Prochaska, J. X. 2005, ARA&A, 43, 861
Wolfe, A. M., & Prochaska, J. X. 2000, ApJ, 545, 591
Wolfe, A. M., Turnshek, D. A., Smith, H. E., & Cohen, R. D. 1986, ApJS, 61, 249